Universiteit Utrecht

Faculty of Geosciences
Earth Sciences
Master's thesis

Real-time drought and landslide monitoring in the Trishuli catchment, Nepal

Methodology and visual output for agricultural water availability and rainfall-induced landslide risk monitoring

Myrthe Leijnse
Student nr. 5738091

First supervisor: prof. dr. Walter Immerzeel
Second supervisor: MSc. Jakob Steiner
1st of April 2021

Rainfall-induced landslide that occurred on the 9th of July 2020 resulting in 23 casualties in the Sindhupalchok district, Central Nepal (left) (Nepali Times, 2020), and a Nepalese farmer cleaning his rice field after failed production due to a local drought in 2020 in the Narainapur district in West Nepal (right) (Eco-Business, 2020).

Abstract

Its high-relief topology, active seismic zone, and intense summer monsoons make Nepal very prone to the occurrence of multiple hazards, among which droughts and landslides (MoHa, 2019). The impact of droughts on the food security and economic development in Nepal is considerable since 65% of the households relies on rain-fed farming (FAO, 2020). Also, landslides have a large impact on the liveability in Nepal, causing considerable economic losses and fatalities every year (Petley et al., 2007); in 2017 and 2018 a total of 484 landslides were reported in Nepal, leading to 161 casualties and an economic damage of 1.6 million USD (MoHa, 2019). To improve drought and landslide risk awareness and preparedness, real-time monitoring of these hazards is necessary. Although many systems monitoring these hazards have been developed and implemented, these systems or their applications often only provide hydrometeorological information displayed on low spatial resolution. There is, however, a need for information that is comprehensible, directly applicable, and, therefore, helpful to drought and landslide risk awareness and early warning on local scale. Therefore, this study has investigated methodologies and visual output for a multi-hazard monitoring model that provides accessible information on agricultural drought occurrence and rainfall-triggered landslide potential in the Trishuli river basin of Central Nepal. These methodologies use meteorological variables at point scale obtained from ECMWF's ERA5 product that is downscaled with meteorological station measurements at different locations throughout the catchment area. For the monitoring of drought impact on rice, wheat, and maize production a visualisation is developed, indicating crop seasonal water availability based on the estimation of Makkink evapotranspiration and a subsequent climatic water balance. Landslide risk has been estimated by comparing the daily index of antecedent rainfall (ARI) to a threshold of extreme antecedent conditions. Although inaccuracies exist for these methods in establishing drought and landslide extent or potential, all methodologies are easy to implement and provide comprehensible insights on landslide or drought occurrence on station scale. Therefore, it is suggested to apply the developed methodologies to real-time or forecasting meteorological measurements to provide real-time monitoring and early warning of landslide and drought occurrence in Central Nepal.

Keywords: Rainfall-triggered landslides; Droughts; Central Nepal; Trishuli; Hazard monitoring

Table of contents

1. Introduction

Nepal is highly susceptible to multiple hazards (Figure 1.1) due to its diverse topography reaching altitudes of above 8000 m to below 100 m, and its great variety of climatic conditions within a short distance of 200 km from the northern to the southern border (Karki et al., 2016; MoHa, 2019). Every year thousands of Nepali are killed by natural disasters; between 2015 to 2018 this number went up to over 10,000 casualties (MoHa, 2017, 2019). Moreover, large economic and environmental losses are caused by natural disasters in Nepal. Protection from natural disasters is often lacking due to inadequate understanding or implementation of disaster risk management (Kafle, 2017). Two hazards that have a major impact on the quality of life and economic development in Nepal are droughts and landslides. So, even though other disasters such as flooding and earthquakes occur frequently and have a large impact in Nepal, this study will focus on landslide and drought hazards.

1.1 Definitions of drought and landslides

A drought is a prolonged and regionally extensive occurrence of below average natural water availability. It often propagates through the water cycle and can occur in three different stages (KNMI, 2018; Tallaksen & Van Lanen, 2004). Droughts usually start as a meteorological drought, which is a precipitation deficit over a certain area and period of time that is significantly below the long-term average. In combination with high evaporation rates this can cause a deficiency in soil moisture, also referred to as an agricultural drought when there is insufficient soil moisture available to support crop growth. When droughts are very persistent over a large part of a catchment, groundwater and streamflow levels will decrease, leading to a hydrological drought. Droughts are recurrent phenomena of any climate type and may be exacerbated by anthropogenic activity through climate change, land use change or water use (Van Loon et al., 2016; Vogt et al., 2018).

On the other hand, when the precipitation intensity or duration is very high, landslides may be triggered. Landslides are natural geomorphological processes that shape the landscape, where mass of soil or rocks move down a slope under the influence of gravity

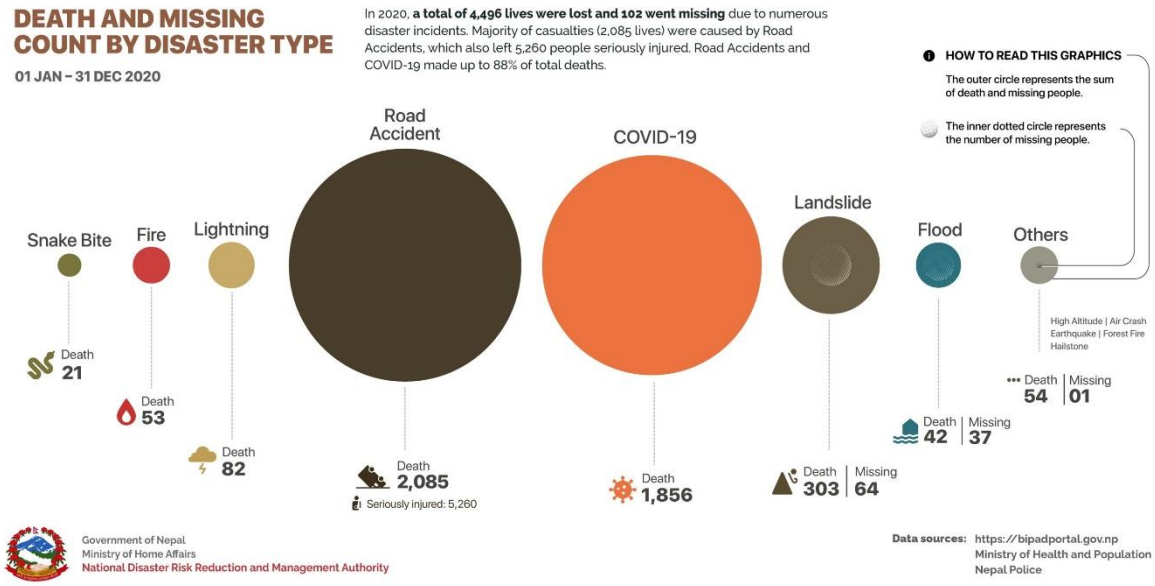

Figure 1.1 Death, missing and injury count of disasters in Nepal in 2020 (BIPAD, 2020).

(Bogaard & Greco, 2015). Landslides occur with different sizes and velocities. Therefore, they are defined into classes that differentiate between material type and soil movement mechanisms. The risk of a landslide increases when its velocity and runout distance are larger, and when the failing slope is in close proximity to residential areas and road structures, increasing the vulnerability of property and inhabitants in the region (Morello et al., 2013). Landslides can be initiated by different factors, such as rainfall, earthquakes, volcanic activity, fluvial processes or glacial retreat, and are often exacerbated by anthropogenic activities (Sidle & Bogaard, 2016). Rainfall and snowmelt inputs are, however, globally the most important trigger of landslide occurrence (Petley et al., 2005), and this is also the case in Nepal (Dahal & Hasegawa, 2008). Therefore, this study will mainly consider rainfall-induced landslides.

The physical mechanism that causes landslides initiated by rainfall is the reduction of shear strength in a soil due to an increased buoyancy force that is exerted by soil water in the saturated zone (Bogaard & Greco, 2015). The shear strength can also be decreased by a reduction of soil suction in the unsaturated zone in combination with increased weight of infiltration water, although it is still uncertain whether this contribution is significant (Bogaard & Greco, 2015; Sidle & Bogaard, 2016). The failure plane of rainfall-induced landslides is often located at shallow depth of a hydraulic discontinuity, resulting in rapid shallow landslides that are relatively more hazardous.

1.2 Droughts and landslides in the Trishuli catchment

The Trishuli River is one of the major tributaries of the Narayani river system that runs through different physiographical regions in Central Nepal from the high Himalayan mountains in the north to the flatlands of the Terai in the south, with the hilly Siwaliks in between (Figure 2.4). The lower part of the drainage system is densely populated with a total population of about 1.2 million in the surrounding districts (Central Bureau of Statistics, 2011), and it contains important highways that connect the capital Kathmandu to other parts of Nepal and China. The lands among the lower elevations of the Trishuli are predominantly used for agricultural purposes (ICIMOD, 2017), and the majority of the inhabitants earn their income from agricultural and livestock proceeds (Dahal et al., 2016). The relatively dense population and extensive agricultural land use make the area vulnerable to both landslides and droughts. Future population growth, environmental degradation and climate change are expected to exacerbate the occurrence and impact of these hazards, making the region even more vulnerable to these disasters (MoHa, 2019).

1.2.1 Drought occurrence and impact in the Trishuli catchment

Nepal may not be considered as most drought prone in Asia. Droughts in Nepal are, however, very important climatic extremes considering their economic damage (Bhandari & Panthi, 2014). Moreover, droughts are expected to become more severe due to global warming (Trenberth et al., 2014), which is also predicted for Central Nepal (Dahal et al., 2016). The Nepalese agriculture is mainly rain-fed and thus very dependent on the summer monsoon (Dahal et al., 2016). Rain-fed farming requires crop planting schedules that coincide with rainfall, so that crops receive sufficient water at their critical growth stages (Ghimire et al., 2010). Rice, maize and wheat are the three main crops that are produced in the districts along the Trishuli river, with a yearly production of approximately 289,000 t of paddy, 197,000 t of maize and 63,000 t of wheat (ICIMOD, 2017).

A decrease in agricultural production due to water stress can cause substantial economic losses in Nepal, since it accounts for 35% of the nation's total GDP (FAO, 2020). Moreover, 64% of the total population relies on their crop yields. Therefore, a decrease in crop yield related to drought occurrence severely affects the nations food security, which is already at a poor state. In 2020, for example, the food production was above average, but about 2.8 million Nepalese people still lived with food insecurity, which accounts for 10% of the total population (FAO, 2021). This is expected to rise in the near future due to COVID-19 related economic decrease (FAO, 2021). On a long-term time scale food demand is expected to increase due to population growth while climate change is expected to reduce crop yields in Nepal, which raises pressure even more on the agricultural production (Bocchiola et al., 2019).

Over the last 20 years multiple droughts have occurred in Central Nepal, of which the droughts during the winters of 2006/2007 and 2008/2009 were most severe, affecting over 500,000 people (EM-DAT, 2020). The drought during the winter of 2008/2009 caused a decrease of 50% in wheat production compared to the previous year (Wang et al., 2013), which had a negative impact on the nation's food security. Resilience of farmers to droughts is low due to irrigation limitations of the Nepalese government and water use conflicts that may occur (Ghimire et al., 2010). The most recent drought occurred during the summer of 2015, which also severely impacted crop yields (Hamal et al., 2020).

1.2.2 Landslide occurrence and impact in the Trishuli catchment

The geological setting, steep terrain, high seismic activity, and intense monsoon season make the Trishuli catchment very prone to the occurrence of landslides (Section 2.3). In Nepal, the annual mean rainfall is between 1500 and 2500 mm, and more than 80% precipitates during the summer monsoon (June-September), making the annual rainfall very unevenly distributed. Also, the daily rainfall intensities can be extremely high, 10% of the annual mean rainfall may occur within a day (Shrestha, 2000). This unevenly distributed rainfall pattern is the main reason for the large amount of rainfall-induced landslide occurrences in Nepal (Dahal & Hasegawa, 2008). Between 2004-2016 Nepal accounted for 10% of the fatal rainfall-induced landslides that occurred globally, making the mortality risk for landslides in Nepal extremely high (Froude & Petley, 2018). This high mortality risk can be related to the lack of appropriate policies, operational frameworks and early warning systems for disaster risk reduction (Kafle, 2017).

Since the disastrous 2015 Gorkha earthquake in Central Nepal, the landslide risk has been elevated in the region (Figure 1.2) and is expected to remain elevated for the coming years (Rosser et al., 2021). The reactivation of landslide hazards during strong monsoons is mainly responsible for this increased trend in landslide risk. Also, change in land use combined with extensive and often informal road construction projects on hillsides have contributed to this increasing trend in landslide occurrence over the recent years (McAdoo et al., 2018; Muñoz-Torrero Manchado et al., 2021; Petley et al., 2007; Rosser et al., 2021). In 2017 and 2018 a total of 483 landslide events occurred in Nepal with 161 casualties and an economic loss of 1.6 million USD (MoHa, 2019). In the Trishuli catchment the Nepalese police reported a total of 26 landslides during the monsoon season of 2020. These landslides took the lives of 9 residents and destroyed 14 houses (Government of Nepal, 2021).

Figure 1.2 Photographs of landslides caused by the Gorkha earthquake in 2015. (a) Shallow landslides along the Trishuli River between Nuwakot and Rasuwa Ghadhi and (b) a rockfall blocking the road between Kathmandu and Rasuwa Ghadhi (Regmi et al., 2016).

1.3 Drought and landslide monitoring

Monitoring and prediction of droughts could improve water resources management by indicating potential precipitation shortages. Subsequently, the vulnerability of crops during their different development stages can be considered, and effective adaptation and mitigation strategies can be implemented (Bhandari & Panthi, 2014). To assure a successful drought preparedness, real-time drought monitoring is necessary, allowing for an immediate anticipation on concurrent moisture deficits.

Currently, the most widely used method for drought estimation is the use of drought indices, such as SPEI and RDrI-Agri (Section 2.1) (Beguería et al., 2014; Vogt et al., 2018). Droughts estimated by these global products are displayed in real-time through online web tools. These tools, however, are of very low spatial resolution and do not represent drought impact on local scale. On smaller scale (South Asia) drought monitoring systems are available as well (Aadhar & Mishra, 2017; Takeuchi et al., 2015), although these remain coarse in their spatial scale, thus not suitable for decision making in water management and agriculture in Nepal.

Also, real-time monitoring of rainfall-induced landslide risk will enhance the sustainable development and liveability of the region. Continuous monitoring of landslide potential will improve the prevention of future casualties and damages caused by the rainfall-induced shallow landslides. Therefore, the implementation of an effective landslide early warning system (LEWS) based on real-time data on basin scale will allow for mitigation of landslide risks.

LEWS that are currently operating are mainly based on rainfall thresholds (Section 2.2). Since many different triggering and disposing factors are involved with the occurrence of rainfall-induced landslides, different types of rainfall thresholds have been developed in previous work for different regions around the world (Guzzetti et al., 2008). Implemented early warning systems in Nepal range from local slope-stability measuring systems (Thapa & Adhikari, 2019) to landslide risk maps coupled to meteorological rainfall measurements (BIPAD, 2020). Although the latter has potential to operate as a nationwide landslide early warning system, it currently only provides a landslide susceptibility map that is unrelated to real-time precipitation measurements.

These operating monitoring systems often only provide the real-time meteorological data, or an index linked to hazard occurrence, whereas for decision making on local scale computed derivatives related to hazards are more convenient, such as water availability for crop production. Moreover, the observation networks are usually limited in developing countries such as Nepal. The TAHMO[1] and REAMO[2] initiatives aim to establish extensive networks of meteorological observations and provide informative applications on climate change, agriculture, and early warning in Africa and High Mountain Asia, respectively.

1.4 Objectives

To improve natural hazard awareness in the Trishuli catchment this study aims to investigate methodologies and generate visual output for a multi-hazard monitoring model that provides information on agricultural drought occurrence and rainfall-triggered landslide potential in the Trishuli catchment. So, this paper only focusses on hazard risk from drought and landslide occurrence, and disregards other hazard types although these also occur regularly and have large impacts. The methodology will be developed using a global reanalysis product that is downscaled with data of meteorological measurements within the basin, which prevents an overgeneralization of point data in a geographically complex terrain. Due to the availability of the meteorological datasets in (near) real-time, the methodology can potentially be used for publicly available mobile applications that provide real-time monitoring of drought and landslide occurrence, supporting the local communities. Therefore, the visualisation should be relevant to the needs of the local population and easy to interpret. These methodologies will serve as preparatory work for future development of mobile applications on drought and landslide risk in Nepal for the REAMO[2] initiative.

The main objective has been divided in three subgoals that will be applied to the study area of the Trishuli catchment using publicly available ERA5 reanalysis data in combination with meteorological observations. These goals aim to (a) analyse the suitability of the dataset for the estimation of evaporation rates and precipitation deficits for drought monitoring of rice, maize, and wheat production; (b) analyse the suitability of the dataset for the estimation of rainfall-induced landslide risk for landslide monitoring at station scale; (c) develop novel visualisations to display information on landslide and drought potential in an accessible format, meeting the needs of the local population.

[1] tahmo.org
[2] reamo.org

2. Previous work and regional setting

2.1 Monitoring of droughts

Droughts are likely the most difficult natural phenomena to estimate due to their complexity and unpredictability. The onset of a drought is difficult to detect due to its slow development and the high complexity of physical processes involved, which often relates to variability in climatic oscillations. Therefore, monitoring of the onset, progress and extent of a precipitation deficit can enhance drought preparedness and mitigation (Morid et al., 2006).

2.1.1 Drought indices

The most widely used method for monitoring drought occurrence is the computation of a drought index. These indices simplify complex drought phenomena by relating the sensitivity of droughts to surface biophysical or hydro-climatical variables, which include precipitation, climatic water balances, soil moisture, vegetation, land surface temperature and albedo (Ghulam et al., 2007; Vogt et al., 2018). These factors are often obtained from meteorological station data, while more recently remote sensing techniques have been developed. The particular method used for calculating a drought index is dependent on the drought type that is considered (Section 1.1) (Vogt et al., 2018).

The most popular drought indicators are the standardized precipitation index (SPI), standardized precipitation evaporation index (SPEI) (Vicente-Serrano et al., 2010) and the Palmer drought severity index (PDSI) (Palmer, 1965), developed for meteorological drought and soil moisture drought analysis, respectively (Vogt et al., 2018). The PDSI calculates a water balance that includes precipitation, moisture supply, runoff and evaporation in a soil model estimated by meteorological observations. The PDSI is considered as one of the most comprehensive drought indices (Ghulam et al., 2007). A disadvantage of the index is, however, that its calculation is complex, which may lead to difficulties with its interpretation (Guttman, 1998). SPI and SPEI are also based on meteorological data. SPI measures a precipitation deficit or surplus from precipitation data only while SPEI estimates drought occurrence with a simplified calculation of a climatic water balance, i.e., precipitation minus reference evapotranspiration. This water balance is then calculated over a certain period of time and standardized so that it becomes comparable on larger scales in space and time.

2.1.2 Estimation of evapotranspiration for drought occurrence

Most issues with the drought indices, such as SPEI, are associated with the approach used for the estimation of evapotranspiration, since direct measurement of this variable is not straightforward and always requires calculation (Allen et al., 1998). For the calculation of evapotranspiration, a distinction has been made between reference evapotranspiration (ET_0) and actual evapotranspiration (ET_a). ET_0 refers to the total atmospheric water demand assuming unlimited access to water resources, while ET_a refers to the atmospheric water demand that can be accounted for by the water availability. ET_a is, however, a poor indicator of drought stress, since it does not represent the response of vegetation on drought stress (Beguería et al., 2014). The difference between precipitation (water availability) and ET_0 (water demand) gives a more appropriate indication of drought occurrence and is, therefore, predominantly used in estimation of drought occurrence. Many different models have been developed to estimate potential evaporation. Liu et al., (2017) have compared 16 different evaporation (ET_0) estimating models to

lysimeter ET_0 measurements, where the models combining temperature and radiation observations performed better than models using temperature or radiation only.

The most recent version of the most common drought index, SPEI, uses the physically-based Penman-Monteith (PM) equation (Monteith, 1965; Penman, 1948) to compute ET_0, which gives a more accurate estimate of ET_0 than previous versions (Mukherjee et al., 2018). This method requires an extensive dataset on meteorological climate variables, such as wind speed, relative humidity, and solar radiation. When measurements of these variables are not available, the Hargreaves method (HG) is alternatively used (Hargreaves & Samani, 1985). This equation only relies on daily maximum and minimum temperatures. An alternative equation that calculates ET_0 is Makkink, which requires slightly less input than PM but more than HG. This method relates daily reference evaporation to incoming solar radiation (Hiemstra & Sluiter, 2011).

The ET_0 calculated from these methods represents solely the climatic demand on evaporation, since it is calculated using meteorological factors alone. Therefore, these methods approximately represent the potential evaporation from a grass field. The FAO have defined two more forms of ET that include crop type, crop development and management practices to make ET more representable for specific agricultural fields (Allen et al., 1998). These are crop evapotranspiration under standard (optimal) and non-standard conditions and are represented in a dimensionless crop factor (K_c). This crop factor is obtained most accurately through field surveys or remote sensing (Allen et al., 1998), hence many studies have conducted to do so (Bhandari, 2011, 2012; Bhandari & Kayastha, 2012; Mokhtari et al., 2019).

2.1.3 Plant phenology: growing degree days estimation

Monitoring of plant growth allows for an improvement in crop management for more efficient production. The development of plants mainly depends on temperature, where a certain amount of heat is required for a plant to reach a certain growth stage. Plant management decisions are, however, occasionally based on calendar dates instead of observed temperatures. This may lead to early or delayed crop management practices. In central Terai of Nepal, for example, winter crops (maize and wheat) are occasionally planted too late in the season, resulting in reduced yields (Amgain, 2011, 2013). Growing degree day (GDD) models have been developed that link plant growth stages to accumulated heat values (Miller et al., 2001). This accumulated heat is determined with crop specific developmental threshold temperatures (Figure 2.1). From the accumulated GDD values the phenology of crops can be estimated at certain thresholds, e.g. a threshold of 2793 GDD to reach the maturity stage of a rice cultivar (Karki & Amgain, 2015).

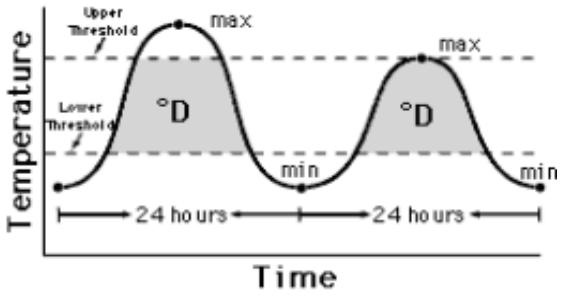

Figure 2.1 Temperature timeseries with minimum and maximum temperature thresholds and corresponding GDD (Miller et al., 2001).

Plant development is, however, also affected by soil moisture availability since water stress at various growth stages may diminish plant growth. Also, the germination of seeds requires an initial amount of water. Rice cultivation in Nepal is an example of a crop which growth is dependent on rainfall patterns and susceptible to drought stress (Karki & Amgain, 2015; Serraj et al., 2009). Rice is most vulnerable to water stress at its flowering stage (Pandey & Thongbam, 2014). The water availability is, however, disregarded in a GDD model as it assumes sufficient moisture available. The GDD model can, however, estimate when the drought sensitive stages of the plant development process occur (Dalhaus et al., 2018). When the water availability is known at these growth stages, measures against drought stress occurrence (irrigation) can be implemented, if necessary. Therefore, monitoring of water availability in combination with plant development is an effective approach to estimate when crop management practices are necessary.

2.1.4 Current drought monitoring practices in Nepal

2.1.4.1 Operational drought monitors on global scale

Multiple drought monitoring systems are operational at global scale. Following the SPEI method (Beguería et al., 2014) an online web tool has been developed, offering near real-time data on global drought occurrence on 1 degree spatial scale and a monthly time resolution available at spei.csic.es. The evaporation calculation is based on the Thornthwaite ET_0 model since real-time data on climate variables other than temperature is often lacking at global scale. Another monitoring system is the JRC Global Drought Observatory (GDO), which also observes drought occurrence in real-time (edo.jrc.ec.europa.eu/gdo/). The monitor estimates the Risk of Drought Impacts for Agriculture (RDrI-Agri), an indicator of drought impact on agriculture that is obtained from meteorological, soil moisture and vegetation greenness combined with vulnerability and exposure factors (Vogt et al., 2018). The spatial and temporal resolution of these global systems is, however, too poor to indicate drought impact on river basin scale.

2.1.4.2 Operational drought monitors on local scale

On local scale a drought monitoring system (DMEWS) based on satellite imagery is operational for drought early warning in Nepal and other Asian Pacific countries available at wtlab.iis.u-tokyo.ac.jp/DMEWS/Nepal/ (Takeuchi et al., 2015). It estimates monthly and annual information on meteorological drought occurrence on a 10 by 10 km grid scale based on the Keetch-Byram Drought Index (KBDI) (Keetch & Byram, 1968). This index estimates the dryness of the upper soil by assuming 8 inches of soil moisture available for vegetation uptake. It is computed with daily precipitation rates and a drying factor that increases with higher daily temperatures. A scale between 0 and 800 indicates to what extent a soil moisture deficit is present, where 0 represents no deficit and 800 a completely dry soil. The resolution of this drought monitor, however, remains too coarse to contribute to decision making at sub-basin scale.

In 2017 a higher resolution (0.05°) near real-time drought monitoring system has been developed to allow for drought information on local scale in South Asia (Aadhar & Mishra, 2017)[3]. In this system bias-corrected temperature and precipitation data has been used to estimate both SPI and SPEI, where for the SPEI estimation the Hargreaves method has been applied to obtain potential evaporation. The work has subsequently been compared to satellite observed drought products (NVDI anomalies). Although there is much

[3] available at sites.google.com/a/iitgn.ac.in/high_resolution_south_asia_drought_monitor/drought-early-warning-system

potential in the high-resolution dataset for drought monitoring at sub-basin scale in near real-time, the work is still in an experimental setting and not functional in real-time yet.

On a national scale many drought impact assessments have been conducted after the occurrence of a severe drought event (Bhandari & Panthi, 2014; Dahal et al., 2016; Shakya & Yamaguchi, 2010). A national real-time monitoring system that is useful for decision-making in water management and agriculture is, however, still non-existent in Nepal.

2.2 Monitoring of landslides

Since the 1970s rainfall has been identified as a main contributor to landslide occurrence (Guzzetti et al., 2020). The challenge with the estimation of landslide occurrence is that not all large precipitation events result in slope failure, meaning that the relation between precipitation and landslide occurrence is not straightforward. While rainfall may be the triggering factor of landslide occurrence, there are also other causal factors involved that relate to slope destabilization on a larger temporal and spatial scale (Bogaard & Greco, 2015). For rainfall-initiated landslides different dynamical processes are involved, such as tectonics, soil weathering, geomorphic changes and vegetation (Figure 2.2) (Sidle & Bogaard, 2016). The relation between the long-term causal factors and slope failure is, however, complex, and not known in detail. Physical process-based models that include these dynamical processes exist, but their practical application for LEWS is bounded to small areas due to the large effort and data demand (Bogaard & Greco, 2018). Therefore, the estimation of landslide occurrence due to rainfall often relies on empirical relations and field observations.

2.2.1 Rainfall thresholds

The most common method to assess rainfall-induced landslide hazards is the heuristic approach of rainfall intensity-duration (ID) thresholds, which determine the minimum intensity or duration of rainfall that is necessary to trigger a landslide. The compilation of an ID threshold is based on the analysis of precipitation intensity and duration, and the corresponding landslide occurrence. This requires a landslide inventory and precipitation measurements that are spatiotemporally of high quality. These empirical thresholds are popular because they can be applied to large regions and the interpretation of their outcome, a single graph, is relatively easy (Thomas et al., 2018).

Rainfall ID curves have been determined on global scale by many studies (Guzzetti et al., 2008), and Dahal & Hasegawa (2008) estimated ID thresholds for landslides in Nepal using rainfall data in proximity to 193 landslide events (Figure 2.3). This threshold relation has, however, only been compared to thresholds in other regions of the world, which is not an appropriate validation method since rainfall ID thresholds may differ greatly for different climatic and physiographic regions. The validation of ID curves by, for example, a contingency matrix, is essential for obtaining an accurate rainfall ID (Segoni et al., 2018). The performance of this rainfall threshold for estimating landslide occurrence by Dahal & Hasegawa (2008) has thus not been evaluated. It is, therefore, uncertain to what extent this threshold is reliable when applied to a LEWS in Nepal.

Rainfall thresholds may contain errors in predicting landslides since they are only a simplified empirical relation between rainfall and landslide occurrence. For a more robust assessment the hydraulic, physical and mechanical terrain characteristics, and the factors that describe the geomorphology should be involved (Figure 2.2) (Dahal & Hasegawa, 2008; Sidle & Bogaard, 2016). Antecedent rainfall conditions are often acknowledged as a

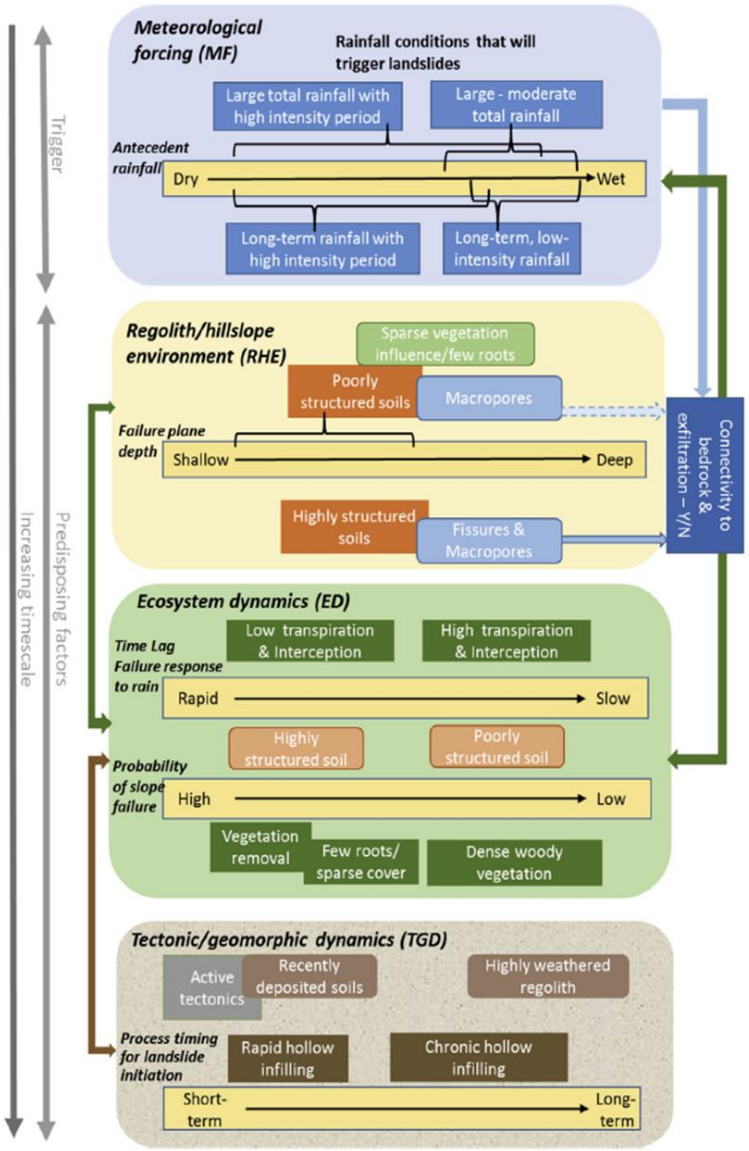

Figure 2.2 Triggering and predisposing factors of rainfall-induced landslides and corresponding depth, probability, or timing of landslides. The bright colours indicate the main processes within a system and light colours are other indirect processes involved (Sidle & Bogaard, 2016).

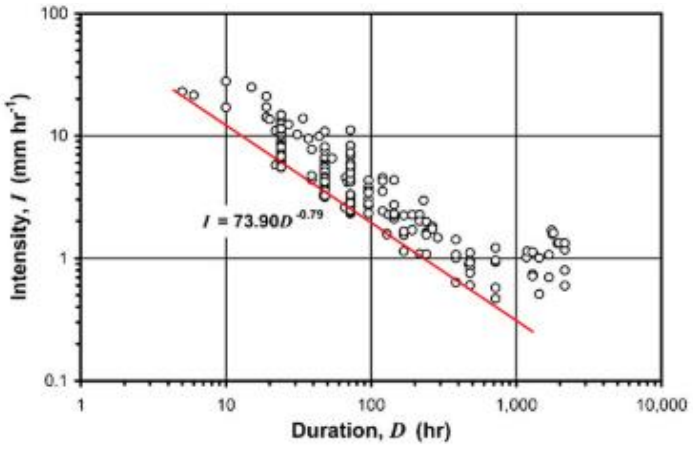

Figure 2.3 Rainfall ID curve (red line) and observed rainfall intensities and durations per landslide event (dots) for the Nepal Himalaya as estimated by Dahal & Hasegawa (2008).

key process for identifying rainfall-landslide relations (Dahal & Hasegawa, 2008; Guzzetti et al., 2008; Mathew et al., 2014). Nevertheless, causal factors such as hydrology are often disregarded in estimating ID thresholds, where the focus relies mainly on the triggering rainfall events instead of the causal antecedent conditions. This is also the case for Dahal and Hasegawa's threshold in Nepal. Therefore, alternative approaches have been suggested using hydro-meteorological thresholds, where proxies for antecedent soil water content are involved (Bogaard & Greco, 2018). Attempts have been made to develop these hydro-meteorological thresholds by involving in situ or remotely sensed soil saturation and altering ID thresholds through incorporating antecedent rainfall conditions (Marino et al., 2020; Mirus, Becker, et al., 2018; Mirus, Morphew, et al., 2018; Thomas et al., 2019), e.g. 15-day average antecedent saturation (Mirus, Becker, et al., 2018). Landslide early warning systems that include these antecedent conditions significantly exceeded the performance of rainfall-only thresholds (Mirus, Becker, et al., 2018). When comparing different sources of antecedent soil moisture, the thresholds based on in situ hydrologic data outperformed the satellite-based data, due to an overestimation of soil moisture by the remotely sensed data (Thomas et al., 2019).

2.2.2 Current landslide monitoring systems in Nepal

2.2.2.1 Operational landslide monitors on global scale

A LEWS that is currently operational is the global LHASA model of Kirschbaum & Stanley (2018) which uses a threshold for rainfall-induced landslide occurrence that includes antecedent moisture conditions. This model uses the antecedent rainfall index (ARI) that computes a weighted average rainfall from the 7 most recent days, where the weight increases towards the most recent date. The index operates as a general indication of soil moisture storage present. When rainfall is so persistent that the storage capacity is exceeded and overland flow occurs, the calculated index will, however, overestimate the amount of soil moisture, since the index does not account for this process (Glade et al., 2000). The LHASA system is of low spatial and temporal resolution. As a result, local precipitation features and short peak rainfall intensities are masked out, making the global system less appropriate to operate as real-time LEWS for the Trishuli catchment.

2.2.2.2 Operational landslide monitors on local scale

Landslide early warning systems in Nepal are often project-based and location specific (Kafle, 2017). An example of such a local LEWS in the Nepalese Himalaya that has been successfully piloted by Thapa & Adhikari (2019) is the community-based LEWS in the Dolakha district, Central Nepal. The system operates on field observations of soil moisture and rainfall. A disadvantage is that such a slope stability measuring system requires equipment located on the landslide slope itself that is likely to get damaged during rapid landslide events. This was also the case for this local LEWS in Dolakha (Thapa & Adhikari, 2019), and makes these systems of high maintenance and relatively expensive.

Since summer 2019 the National Emergency Operation Centre of Nepal has been operating a disaster management web portal on national scale (bipad.gov.np/). This system collects and displays the occurrence of different natural and anthropogenic hazards, including floods, earthquakes, and landslides. The application also provides a risk map for earthquake and rainfall-induced landslide occurrence, that is based on rainfall duration thresholds. The risk map does, however, not indicate which exact slopes are prone to sliding, since risk is averaged per ward. Moreover, this system does not take all hazards into account, e.g. a drought monitor is missing.

2.3 Study area

The Trishuli river is located in Central Nepal at a latitude of 27°40 N - 28°14 N, and longitude of 84°20 E - 85°22 E (Figure 2.4). The area of interest covers about 9000 km^2. The Trishuli river is a sub-basin of the Gandaki River Basin, which is again part of the Ganga River Basin. The Trishuli originates in the Tibet Autonomous Region of China and flows in the Narayani River a few kilometres north of Bharatpur. Along the river's valley many terrace plains occur that are densely populated and provide fertile soils for cultivation. The main settlements that are located within the river's catchment are Bidur, Dhunche and Dhading Besi. Major cities Bharatpur and Kathmandu are in close proximity of the catchment. Two important roads that connect the capital Kathmandu with China (northbound) and with Bharatpur and Pokhara (westbound) run along the Trishuli river (Figure 3.1). The connection between Nepal and China will remain important as China's Belt and Road Initiative (BRI) aims to expand trade into Nepal and India, and seeks to invest in Nepalese road construction through the Trishuli catchment, although concerns are present on geo-colonialism from China's side of this project (Shrestha, 2019; Telegraph Nepal, 2020).

The slope steepness varies from flat areas around Bharatpur and Kathmandu to steep gradients in the higher Himalaya, with an average slope of 25° in the study area. The elevation ranges from 65 to 8748 meters (Figure 2.4). The borders of the five physiographical regions align with the major thrust and faults in Nepal (Figure 2.5) (Upreti, 1999). Two of the major thrusts run through the study region: the Main Central

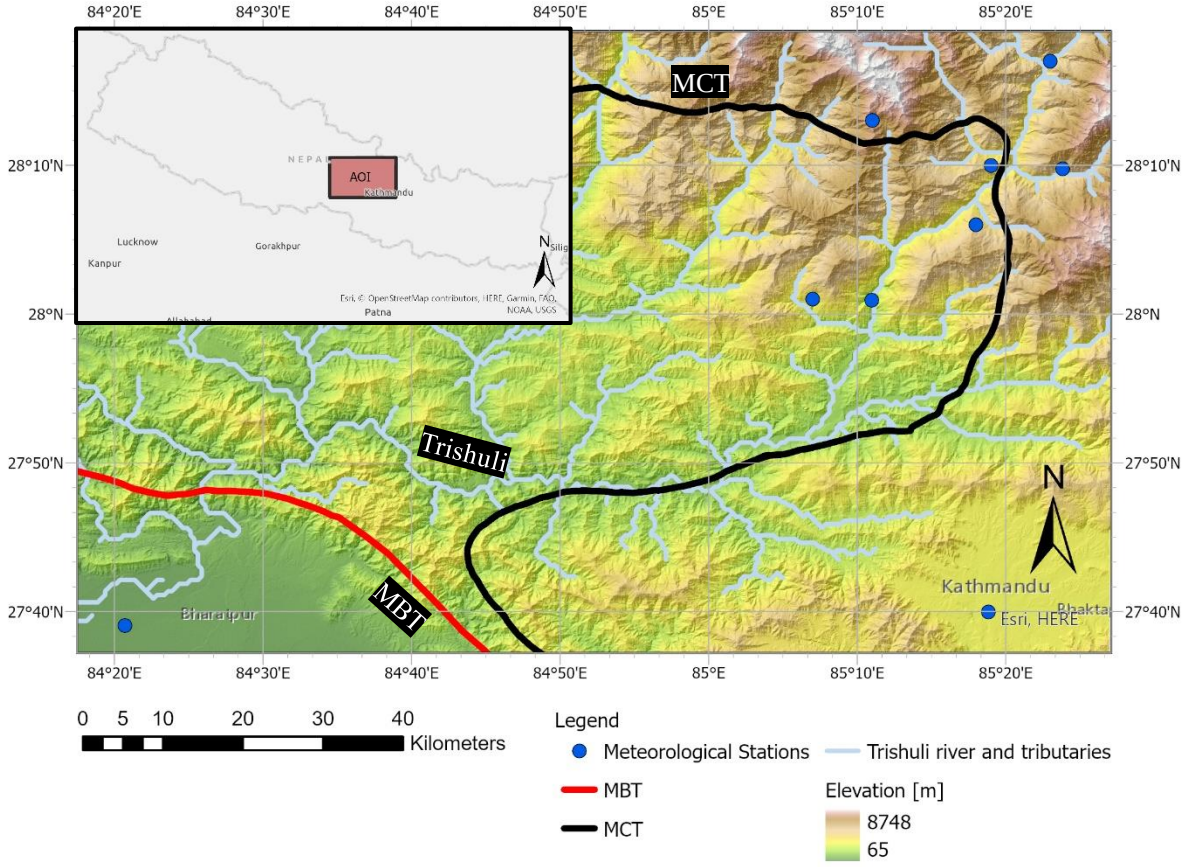

Figure 2.4 Digital elevation map of the area of interest (AOI) including the location of meteorological stations, the Trishuli river and its tributaries, and the approximate location of the main thrusts (MBT and MCT).

Thrust (MCT), which separates the Higher Himalayan Zone from the Lesser Himalayan Zone, and the Main Boundary Thrust (MBT), which is the boundary between the Lesser Himalayan Zone and the Siwalik Zone (Upreti, 1999). Along these thrusts earthquakes commonly occur, such as the Gorkha earthquake in 2015 that had a magnitude of 7.8 on the Richter scale (Regmi et al., 2016).

The study area also comprises different climatological zones, with a very cold polar climate at altitudes above 3000 m, a temperate climate at altitudes between 3000 to 1000 m and a subtropical climate below 1000 m (Karki et al., 2016). The mean annual temperature varies considerably from -8 to 28 °C, where the temperatures range from 6 to 16 °C at the higher altitudes (>2500 m) and from 18 to 28 °C in the Terai region. The average monthly precipitation measured by the meteorological stations in the study area (Figure 2.4) varies from a monthly mean of 0 mm in October to December to 1200 mm in July, although spatial differences are very large.

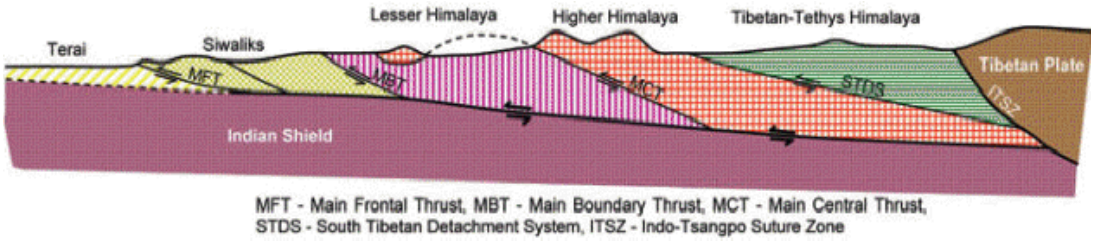

Figure 2.5 Generalized geological cross section of Nepal from south (left) to north (right) including the major faults (Dahal, 2006).

3. Methods

3.1 Data collection

In order to present and validate the methodology, publicly available meteorological reanalysis data is used supported by in situ meteorological station data and a landslide inventory that will be described in the following sections.

3.1.1 Compilation of meteorological dataset

3.1.1.1 Meteorological station data

Four meteorological stations positioned along the Trishuli river provided by the REAMO[2] initiative are used for this study (Figure 3.1). These stations have been operational since February 2020 or earlier, and measure 12 different meteorological variables with a very high temporal resolution of 15-minute time steps (Table 3.1). Some data gaps may occur, e.g. the station at North Betrawati contains major gaps from July 2020 onwards. Additionally, variables measured by five other meteorological stations near the Trishuli river are used, which are available for different time periods and on a different temporal resolution (Table 3.1 & Figure 3.1). These stations only provide data on daily minimum and maximum temperature, and daily precipitation rates.

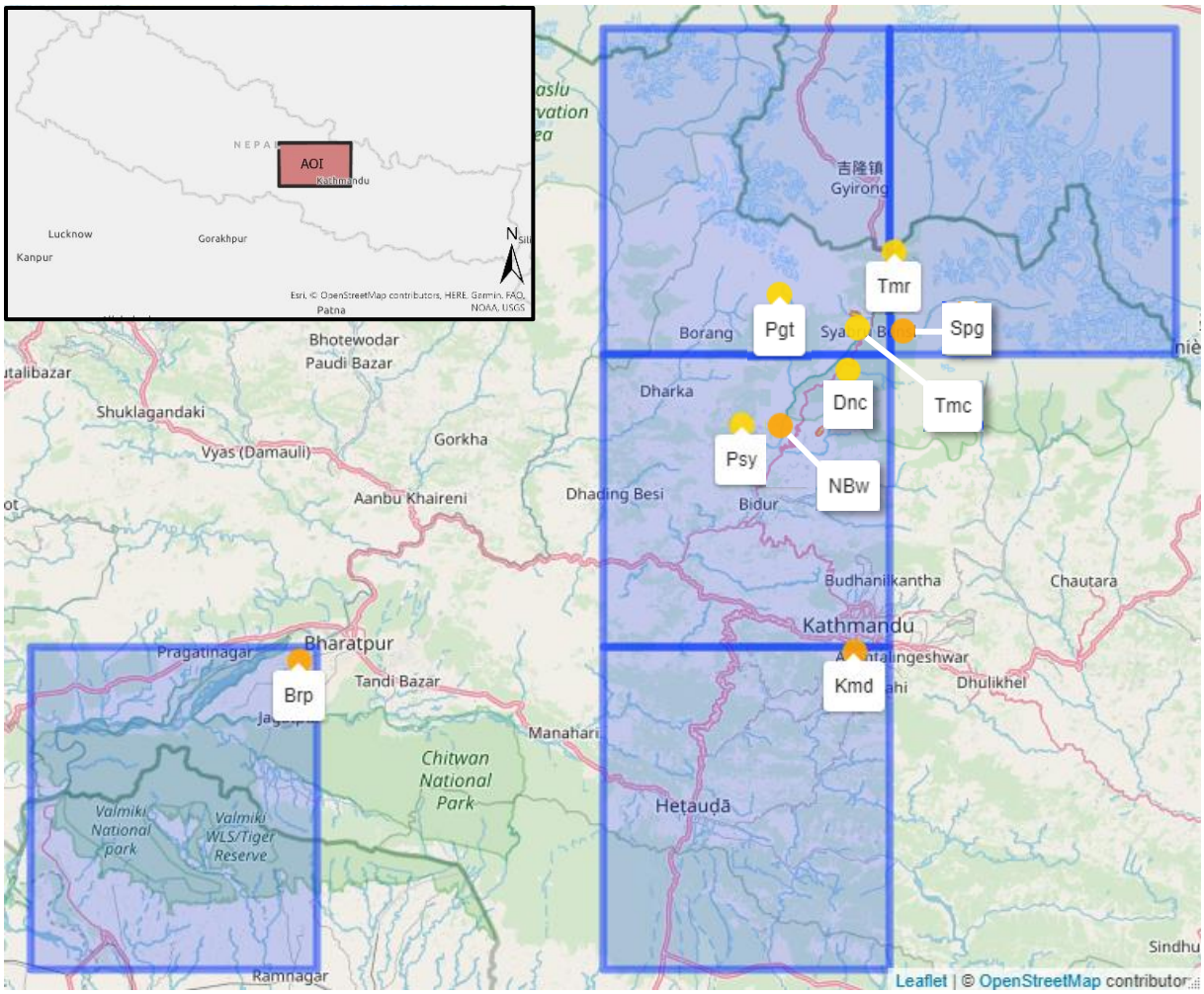

Figure 3.1 Locations of REAMO (orange) and additional (yellow) meteorological stations and the corresponding ERA5 grid cells.

Table 3.1 Characteristics of the meteorological stations in Central Nepal.

Station (abbreviation)	District	Latitude	Longitude	Elevation	Period covered T	Period covered P	Variables measured [a]
Kathmandu (Kmd)	Lalitpur	27.67°N	85.31°E	1330 m	31 Dec 2019 - 6 Dec 2020	31 Dec 2019 - 6 Dec 2020	P, T, R_n, n_{dir}, n, n_{gust}, e_a, P_{atm}, P_{max}, RH_T, L, L_{dis}
North Betrawati (NBw)	Rasuwa	28.02°N	85.18°E	736.3 m	18 Feb 2020 - 31 Dec 2020	18 Feb 2020 - 31 Dec 2020	P, T, R_n, n_{dir}, n, n_{gust}, e_a, P_{atm}, P_{max}, RH_T, L, L_{dis}
Bharatpur (Brp)	Chitwan	27.65°N	84.35°E	160.0 m	18 Feb 2020 - 1 Sep 2020	18 Feb 2020 - 1 Sep 2020	P, T, R_n, n_{dir}, n, n_{gust}, e_a, P_{atm}, P_{max}, RH_T, L, L_{dis}
Sherpagaon (Spg)	Rasuwa	28.16°N	85.40°E	2597 m	31 Oct 2019 - 1 Sep 2020	31 Oct 2019 - 1 Sep 2020	P, T, R_n, n_{dir}, n, n_{gust}, e_a, P_{atm}, P_{max}, RH_T, L, L_{dis}
Timure (Tmr)	Rasuwa	28.28°N	85.38°E	1900 m	1 Jan 2005 - 30 Dec 2015	1 Jan 1986 - 30 Dec 2015	P, T_{max}, T_{min}
Thamachit (Tmc)	Rasuwa	28.17°N	85.32°E	1847 m	-	1 Jan 1986 - 30 Dec 2015	P
Dhunche (Dnc)	Rasuwa	28.10°N	85.30°E	1982 m	1 Jan 1989 - 31 Dec 2015	1 Jan 1986 - 30 Dec 2015	P, T_{max}, T_{min}
Pansayakhola (Psy)	Nuwakot	28.02°N	85.12°E	1240 m	1 Jan 1986 - 30 Dec 2015	1 Jan 1986 - 30 Dec 2015	P, T_{max}, T_{min}
Paigutang (Pgt)	Rasuwa	28.22°N	85.18°E	4091 m	1 Jan 1990 - 31 Dec 1997	1 Jan 1990 - 31 Dec 1997	P, T_{max}, T_{min}

[a] P = precipitation [mm], T = air temperature [°C], R_n = net incoming solar radiation [W/m²], n_{dir} = wind direction [°], n = wind speed [m/s], n_{gust} = gust speed [m/s], e_a = vapor pressure [kPa], P_{atm} = atmospheric pressure [kPa], P_{max} = maximum precipitation rate [mm/h], RH_T = relative humidity temperature [°C], L = lightning activity, L_{dis} = lightning distance [km].

3.1.1.2 Reanalysis data

Most meteorological stations used in this study contain data gaps and may have a short operational period, making the timeseries discontinuous or short. To improve the continuity of these timeseries, a reanalysis product (ERA5) is consulted. The ERA5 reanalysis product of the ECMWF (European Centre for Medium-Range Weather Forecasts) is the result of modelling output that is adjusted by historical observations to give the best model output when compared to the past climate. The data is publicly available at medium scale cell sizes of 0.5° by 0.5° (~30 km) from 1979 onwards through the KNMI/WMO climate explorer (climexp.knmi.nl/). The ERA5 data is obtained for the grid cells corresponding to the locations of the meteorological stations (Figure 3.1) on a daily timescale for four meteorological variables: precipitation (P), incoming solar radiation (R_s), minimum temperature (T_{min}) and maximum temperature (T_{max}).

The spatiotemporal variability in climate variables from ERA5 data is much smoother at its grid box scale than in reality at local station scale (Maraun, 2013). In other words, the resolution of the ERA5 data is too low for implementation on point scale. Another

disadvantageous characteristic of reanalysis data is the so-called drizzle effect. This effect causes that too many days are simulated with very low precipitation rates, while dry days are very uncommon (Maraun, 2016).

To use the ERA5 variables for modelling on point scale a quantile mapping downscaling technique is applied to the data. This method performs a bias correction to the ERA5 output while ensuring realistic daily and interannual variability by matching the distribution of the modelled ERA5 output to a calibration period (Figure 3.2). Quantile mapping also adjusts for the amount of wet days to overcome the drizzle effect (Maraun, 2016). The calibration period is a manually selected part of the observed timeseries that contains the largest continuous timeseries, so without data gaps. This calibration period is retrieved for most meteorological stations, except for the stations at North Betrawati and Thamachit as these stations provided insufficient continuous data. For the other stations, the downscaling procedure resulted in continuous timeseries of P, R_s, T_{min} and T_{max} from 1979 to 2020 on a daily timescale. These timeseries are also available on an hourly timescale for the REAMO stations that measure on a higher temporal scale (Kathmandu, Bharatpur).

3.1.2 Landslide inventory

The landslide occurrences have been reported by the Nepalese police and these are publicly available through the Nepal Disaster Risk Reduction (DRR) portal (drrportal.gov.np/). This data is obtained for all days between 2017 and 2020 which can be found in Appendix A. A total of 124 landslides have been observed in the study area. This landslide inventory indicates the date of occurrence and corresponding municipality. From this the rough coordinates of the landslides have been estimated, such that all single landslide events can be linked to a meteorological station in closest proximity (Figure 3.3). With this inventory a relation between landslides and rainfall at point scale is investigated (Section 4.2.2) and the accuracy of an ARI landslide risk threshold is evaluated (Section 4.2.3).

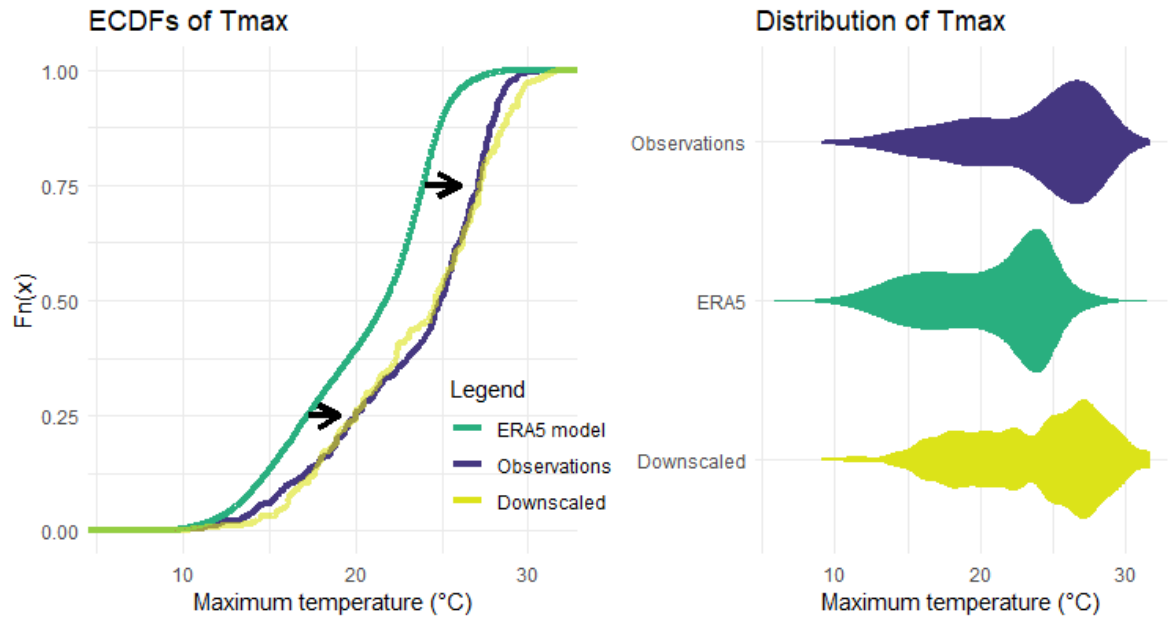

Figure 3.2 Example of the quantile mapping method for T_{max} at the Kathmandu station. The left graph displays the empirical cumulative distribution functions (ECDF) and matching of the ERA5 quantiles to the in situ observations. The right graph gives the resulting distributions of the variable before and after quantile mapping.

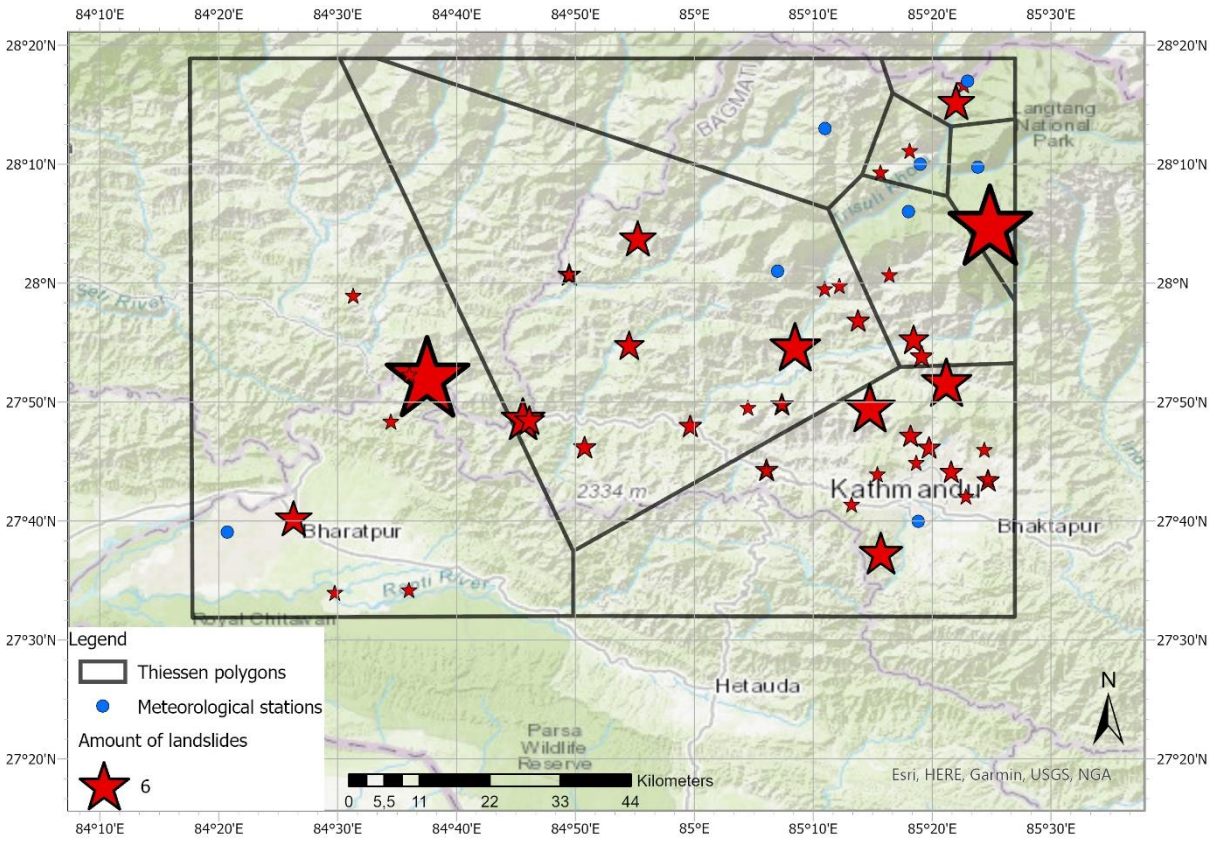

Figure 3.3 Approximate locations and number of landslides reported in the DRR landslide inventory between 2017 and 2020 (red), and the meteorological station locations (blue). The size of the red markers represents the number of landslides that have occurred at that approximate location. The Thiessen polygons represent the boundaries between the areas of closest proximity to the stations.

3.2 Methodology

In this section the methodology to analyse the downscaled reanalysis dataset's suitability for estimating precipitation deficits and landslide risk is explained. The compilation of the meteorological dataset at point scale and further analyses were generated in the R programming language (R Core Team, 2019) and publicly available at [github.com/myrtheleijnse/MasterThesis_REAMO]. A distinction has been made between the methodology with regards to droughts and landslides in the following subsections.

3.2.1 Agricultural drought potential

Since the agricultural sector in Nepal is most severely affected by drought impact, the methods developed in this study are focussed on identifying agricultural droughts (Section 1.1). Consequently, the methodology has been performed on the stations that are most proximate to the agricultural regions in Nepal: Kathmandu and Bharatpur.

3.2.1.1 Analysis temperature, precipitation, and their anomalies

To explore possibilities for drought estimation, the climatic anomalies of the data are assessed by comparing the long-term climate to the monthly observations of 2020 per station. The monthly mean temperature and monthly summed precipitation are estimated for 2020 at both stations and these are compared to the long-term (2000-2020) monthly mean temperature and monthly summed precipitation, respectively. Also, the 90-10th percentiles of long-term monthly temperatures and precipitation are determined to identify extreme values in precipitation (P) and temperature (T) on monthly scale in 2020.

The monthly anomalies (Δ_{rel} and Δ_{abs}) have also been calculated for all years between 2000 to 2020, where the monthly values of both variables were compared to the long-term mean as follows:

$$\Delta_{rel} = \frac{V_m - \mu_m}{\mu_m} \quad (1)$$

$$\Delta_{abs} = V_m - \mu_m \quad (2)$$

Where Δ_{rel} is the monthly anomaly in relative values [%], Δ_{abs} the monthly anomaly in absolute values (mm for P and °C for T), V_m is the mean T or summed P for each month per year, and μ_m is the monthly mean of the respective variable over a period of 2000-2020. As the monthly summed P cannot be below 0, a change of -100% in the P anomaly indicates a month without precipitation. On the other hand, precipitation could change with an infinitely positive percentage, especially when the monthly mean is very close to zero. This would then result in a skewed distribution of precipitation anomalies. Therefore, all changes larger than 100% are grouped as >100% to ensure that extremely low anomalies are not diminished.

3.2.1.2 Analysis of growing degree days and growth stages

To monitor crop development per station, a growing degree day (GDD) model is developed. This model will be applied to the most important crops in the region: paddy, wheat, and maize. The growing degree days are related to the daily mean temperature where high temperatures advance plant growth and low temperatures cause a delay (Miller et al., 2001). The GDDs are summed to give an estimate of the occurrence of certain crop growth stages using Eq. (3).

$$CumGDD(n) = \sum_{i=1}^{n} T_i - T_{base} \quad (3)$$

$$T_i \begin{cases} T_i < T_{base} = T_{base} \\ T_i \geq T_{base} = T_i \end{cases}$$

where T_i is the daily mean temperature (°C) for day i over a period of n days starting at the date of sowing (Mcmaster & Wilhelm, 1997). T_{base} is defined as the daily mean temperature [°C] below which plant growth and development stops. The crops growing in the cool season or in temperate climates usually have a T_{base} of 0°C, which is lower than the T_{base} of tropical crops. Due to lack of information on T_{base} for cultivars in Nepal, T_{base} is set to 0°C for all crops in this study. Upper thresholds also exist, which is the temperature above which plant growth stops, these are however difficult to determine due to their dependence on other environmental conditions (Miller et al., 2001). For that reason, upper thresholds are disregarded as well.

To estimate the growth stage of a crop, the cumulative GDD is compared to GDD thresholds. These thresholds are crop specific and have been determined by previous studies in the Terai of Nepal (Amgain, 2011, 2013; Karki & Amgain, 2015). The GDD thresholds used in this study are displayed in Table 3.2, where the phenological period is divided into three generalized stages: initiation, flowering, and maturity.

Table 3.2 Growing degree days thresholds [°C] for winter wheat, rice paddy and maize per phonological stage and corresponding dates of sowing as estimated in Dhobadi, Nawalpur (rice) and Rampur, Chitwan (maize, wheat).

	GDD threshold [°C] [a]	Growth stage	Sowing date	Reference
Rice	1023	Panicle initiation [b]	15 Jul	Karki & Amgain, 2015
Rice	2028	Flowering	15 Jul	Karki & Amgain, 2015
Rice	2793	Maturity	15 Jul	Karki & Amgain, 2015
Wheat	203	Crown root initiation [b]	1 Jan	Amgain, 2013
Wheat	701	Flowering	1 Jan	Amgain, 2013
Wheat	1071	Maturity	1 Jan	Amgain, 2013
Maize	642	Emergence [b]	1 Apr	Amgain, 2011
Maize	950	Anthesis [c]	1 Apr	Amgain, 2011
Maize	1481	Maturity	1 Apr	Amgain, 2011

[a] Mean GDD threshold as estimated for different cultivars and sowing dates from corresponding reference

[b] Referred to as "initiation" growth stage

[c] Referred to as "flowering" growth stage.

The cumulative GDD is calculated for 2020 and for a long-term reference period to compare the ongoing crop development to previous years. The median, the 10th and the 90th percentiles of cumulative GDD are determined for the reference period of 1999 to 2020. Also, the growth stage development is compared to the daily precipitation rates, because rain distribution has an impact on crop development (Section 2.1.3) (Karki & Amgain, 2015).

As the timing of the transition between different growth stages is determined by when the cumulative GDD exceeds a certain GDD threshold (Table 3.2), the lengths of the crop growth stages can be estimated. These are then displayed in a crop calendar, where the crop development stage is corresponding to when the initial growth is surpassed (a canopy of >10% is reached according to Allen et al., 1998). At the onset of crop flowering the mid-season period starts until crop maturity is reached and harvesting of crops is possible. The end of the harvesting period is estimated as the 30th day after crop maturity has been reached.

3.2.1.3 Analysis of the climatic water balance

To determine whether a period (crop season) is drier or wetter than usual, a climatic water balance is estimated per station location and accumulated over this period. In this water balance only meteorological variables are considered: precipitation (P) and potential evapotranspiration (ET_0). Hydrological variables that are commonly used in water balance estimations, such as runoff, are disregarded in this method since hydrological measurements are not available at the stations. The cumulative climatic water balance is estimated as follows:

$$W(n) = \sum_{t=1}^{n} P_t - ET_{0,t} \quad (4)$$

where W(T) is the cumulative climatic water balance [mm] over a certain season in days (n), P_t the daily precipitation [mm], $ET_{0,t}$ the daily reference evapotranspiration rate [mm] and t the timestep in days. P is obtained from the meteorological dataset and ET_0 is estimated using the Makkink method (Hiemstra & Sluiter, 2011):

$$ET_0 = c * \frac{\Delta}{\Delta + \gamma} * \frac{R_s}{\lambda * \rho} * 1000 \quad (5)$$

with c as a constant equal to 0.65, Δ as the curve of saturation water vapour pressure [kPa/°C], γ as the psychometric constant [kPa/°C], R_s as the daily incoming shortwave radiation [J/m²/day], ρ as the bulk density of water [1000 kg/m³], λ as the heat of vaporization [J/kg] and 1000 as another constant to convert m to mm. The full calculation sheet of Makkink ET_0 with calculations of Δ, γ and λ is displayed in Appendix B. For the calculation of Makkink ET_0 only daily R_s and T_{mean} from the meteorological dataset are required as input.

Many other models exist that estimate ET_0 from meteorological variables, of which some are more complex than others (Section 2.1.2). Due to the lack of long-term data on relative humidity and wind speed, the relatively simple Makkink method is used in this study. This method is also compared to ET_0 calculated using the FAO-56 Penman-Monteith method (Allen et al., 1998) and the Hargreaves method (Allen et al., 1998; Hargreaves & Samani, 1985) (Appendix B). Since not all variables that are necessary for the computation of Penman-Monteith are available in the downscaled reanalysis dataset, the ET_0 has been computed from station measured data. These are available for the Kathmandu station over a period of January 2020 to December 2020 and for the Bharatpur station from February 2020 to September 2020 (Table 3.1).

The cumulative water balance is estimated for the most recent crop seasons in 2020. Subsequently, the median, the driest and wettest year, and the 10th and 90th percentiles have been determined of the cumulative climatic water balance over a long-term historical period (2000-2020). To indicate the cumulative water balance of a reference drought year, the water balance of 2015 is computed as well. The climatic water balance of 2020 is then compared to these reference periods to identify whether the current (2020) meteorological conditions are relatively dry or wet.

3.2.1.4 Analysis of crop specific climatic water balance

Reference evapotranspiration (ET_0) only depends on climatic parameters such as radiation and air temperature, ignoring the land use and environmental conditions of the location (Section 2.1.2). When assessing the evapotranspiration in an agricultural field, the crop type, variety, and development should be considered, since these characteristics may have a significant impact on the evapotranspiration rate. Therefore, the crop evapotranspiration rate under standard conditions (ET_c) is estimated for the winter wheat, maize, and paddy to give a more accurate water balance for agricultural fields. This could then provide information on water requirement in the region during dry periods.

The crop evapotranspiration can be calculated by including crop and air resistance factors, but there is still a lack of information on these parameters for many crops. Therefore, the more simple so-called crop coefficients (K_c) are used to relate reference evapotranspiration (ET_0) to crop reference evapotranspiration (ET_c) Eq. (6) (Allen et al., 1998).

$$ET_c = ET_0 * K_c \quad (6)$$

with ET_c and ET_0 in mm/day and K_c as a dimensionless constant. The crop coefficient depends on variables, such as leaf anatomy, stomatal characteristics, aerodynamic properties and albedo, that differ per phenological stage (Allen et al., 1998). Consequently, the K_c values change throughout the growing season and those used in this study are presented in Table 3.3 (Bhandari, 2011, 2012; Bhandari & Kayastha, 2012). Here the K_c values are given for the growth stages that link to those identified by the GDD model (Section 3.2.1.2).

To estimate the subsequent crop water requirement a crop specific water balance (W) has been calculated and accumulated over the growth season (n) using an equation similar to Eq. (4) in which ET_0 is replaced with ET_c:

$$W(n) = \sum_{t=1}^{n} P_t - ET_{c,t} \quad (7)$$

Again, this crop specific cumulative water balance is compared to the crop specific cumulative water balance of drought year 2015, the long-term (2000-2020) mean, and 10-90th percentiles over the corresponding crop seasons.

Table 3.3 Growth stages and corresponding K_c values [-] for wheat, maize and rice crops as estimated in the Rupandehi district in Nepal.

	Initial [a]	Crop development [b]	Mid-season [c]	Late season [d]	Reference
Wheat	0.34	0.67	0.73	0.06	Bhandari, 2011
Maize	0.11	0.35	1.51	0.34	Bhandari, 2012
Rice	2.92	1.85	0.43	0.12	Bhandari & Kayastha, 2012

[a] Growth stage from sowing to initiation
[b] Growth stage from initiation to flowering
[c] Growth stage from flowering to maturity
[d] Growth stage after maturity.

3.2.2 Rainfall-induced landslide potential

In this study the aim is to identify landslides triggered by rainfall events, therefore extreme rainfall patterns are analysed at all station locations. Subsequently, a landslide-triggering rainfall threshold is applied to the meteorological dataset. The performance of this threshold is then evaluated through the estimation of different performance classifiers.

3.2.2.1 Analysis of maximum precipitation rates

Two different approaches are used to identify the occurrence of extreme rainfall events that may trigger landslides and to identify whether current year (2020) is deviating from previous years. The daily maximum precipitation is used as a proxy for extreme rainfall and analysed on monthly scale.

Firstly, the maximum daily precipitation rates are determined per month for each station in 2020. Also, the maximum daily precipitation per month is estimated for the 20 previous years (2000-2019). This allows for the computation of the mean and 10th-90th percentiles of maximum daily precipitation on a long-term time scale for each station. Subsequently, these statistics derived from long-term conditions are compared to the observed daily maximum precipitation on a monthly basis.

Secondly, the number of days per month during which extremely high precipitation rates occur, are estimated per meteorological station. Precipitation is considered as extremely high when it exceeds the 95th percentile rainfall threshold as obtained from the long-term (1979-2020) precipitation data at the particular station. Subsequently, the number of days that exceed this threshold are summed per month. Similarly, the number of days with extreme precipitation are identified for 2000-2019 and summarized through estimating the mean, 10th and 90th percentiles.

3.2.2.2 Statistical analysis of landslide-rainfall relation

Literature review suggests a relation between precipitation and landslide occurrence (Section 2.2). In this study the goodness of fit for a linear relation between monthly precipitation and number of reported landslides is estimated per station through the calculation of an adjusted R^2. This coefficient shows to what extent the variance of landslide occurrences can be explained by the variation in monthly precipitation.

Moreover, the number of days is counted on which a landslide occurred while any precipitation was observed. From this a percentage is computed of days on which both landslides and precipitation events were present compared to the total amount of days with landslide events per station. Also, the daily maximum rainfall intensity in mm/h is computed and matched to daily landslide occurrence. In this study the rainfall intensity is only estimated for the REAMO stations since the meteorological dataset is not available on hourly scale for all stations (Section 3.1.1.1).

Dahal and Hasegawa (2008) specified an ID threshold according to their precipitation and landslide data that are should be valid over the entire Nepal Himalaya (Section 2.2.1). From the downscaled dataset the intensity and duration of landslide triggering rainfall events is determined to estimate whether these precipitation events exceed the ID threshold of Dahal and Hasegawa. Similar to Dahal and Hasegawa the ID values are determined using the methodology of Caine (1980), where the duration is defined as the duration of the rainfall event prior to landsliding, and the intensity is defined as the average intensity during this rainfall event. Since the hour of landslide occurrence is missing in the DRR landslide inventory, the hour of maximum precipitation intensity is assumed as the moment of landslide occurrence. Again, these calculations are only possible for stations with hourly precipitation data available.

3.2.2.3 Antecedent rainfall index

Many different methods have been developed that compute a landslide-triggering rainfall threshold (Section 2.2.1). The challenge is, however, that it should be representable for the wide range of climates in Nepal that occur within a short longitudinal distance. Moreover, the importance of antecedent rainfall conditions has been emphasized in Section 2.2.1. Therefore, the antecedent rainfall index (ARI) as proposed by Crozier (1999) and Glade et al. (2000), and implemented in the LHASA landslide monitoring model (Kirschbaum & Stanley, 2018) is applied in this study. This index calculates a weighted average of precipitation from the past 7 days including the current day itself [mm]:

$$ARI = \frac{\sum_{t=0}^{6} P_t w_t}{\sum_{t=0}^{6} w_t} \quad (8)$$

with t as the number of days before present, P_t as the precipitation [mm] at day t. The weighted average is calculated with Eq. (9).

$$w_t = (t+1)^{-2} \quad (9)$$

The exponent of w_t (-2) and the window length (7 days) have been calibrated using a global landslide inventory in previous work, where the values with the best predictions were selected (Kirschbaum & Stanley, 2018). The ARI is computed at each station location using the downscaled ERA5 daily precipitation over a period from 1979 to 2020. From this an extreme ARI threshold, which is the 95th percentile of all historical ARI values, is computed for each individual station. The ARI is then estimated for the daily station rainfall of 2017-2020 and this value is compared to the 95th percentile threshold to determine potential rainfall-triggered landslide risk:

$$Landslide\ risk \begin{cases} ARI < P_{95} = No\ risk \\ ARI \geq P_{95} = Potential\ risk \end{cases} \quad (10)$$

where P_{95} is the extreme precipitation threshold [mm]. The landslide risk is subsequently displayed in a calendar.

3.2.2.3 Evaluation of landslide risk estimation

The daily landslide risk calculated by the ARI is evaluated by comparing it to actual landslide days provided by the DRR landslide inventory. A confusion matrix and common performance metrics are obtained (Figure 3.4). These classifiers are calculated for each station where landslides have occurred from 2017 to 2020 in close proximity. Figure 3.3 shows, for example, that nearby the Paigutang station no landslides have been reported over that period, so this station is disregarded.

All performance indicators range from 0 to 1, where 1 is the optimum value (Liu et al., 2021). The TP_{rate}, the so-called *hit rate*, indicates the ratio of actual positives that have been recognised as positive by the ARI. The TN_{rate} is the ratio of actual negatives that have been recognised correctly by the ARI. The precision is the positive predictive value, so the ratio of landslides that are correctly predicted to occur, and the accuracy is the ratio of correct predictions compared to the total amount of predictions.

		True class (landslide inventory)	
Hypothesized class (ARI prediction)	Yes	True Positive (TP)	False positive (FP)
	No	False Negative (FN)	True Negative (TN)
	Σ	Positives (P)	Negatives (N)

$$TN_{rate} = \frac{TN}{TN + FP}$$

$$TP_{rate} = \frac{TP}{TP + FN}$$

$$Precision = \frac{TP}{TP + FP}$$

$$Accuracy = \frac{(TP + TN)}{TP + TN + FP + FN}$$

Figure 3.4 Confusion matrix and most important performance classifiers based on Fawcett, 2006 and Mirus et al., 2018.

4. Results

4.1 Agricultural drought potential

4.1.1 Temperature and precipitation anomalies

Figure 4.1 compares the monthly summed precipitation and mean temperature (2020) to the long-term climatology for the two southernmost stations in the study area. This allows for the identification of seasonal deviations in precipitation and temperature trends. In this case, the 2020 the summer monsoon was relatively strong in Bharatpur and Kathmandu. As Figure 4.1 indicates, the monthly precipitation exceeded or equalled the 10% wettest conditions that were observed between 2000-2020 in June and July. In August, the total amount of rainfall was, however, below the long-term average, which could imply that the 2020 monsoon season had an early ending, although September was relatively wet again. The monthly mean temperatures of 2020 follow a similar trend as the long-term average monthly temperature. The percentile range is relatively small with differences of only 2°C between the 10% warmest and coldest years, meaning that the monthly mean temperature has been stable over the last 20 years. This is also evident in Figure 4.2, where temperature anomalies only deviate ± 20% (2.5°C) from the monthly average mean.

When considering relative change, Figure 4.2 also indicates that negative changes in precipitation anomalies are mainly occurring during the winter season (Nov-Mar) at both locations, whereas the precipitation remains more constant during the monsoon season. The absolute values show, however, that the variability in precipitation is much higher during the summer monsoon than in winter. This is caused by very low long-term monthly mean precipitation in winter, which amplifies relative changes.

Drought years of 2006, 2008/2009 and 2015 (Section 1.2.1) are possibly reflected by a slight increase in winter temperature anomalies. These years are also identified by negative changes in winter precipitation compared to the long-term monthly mean, and even more clear by an absolute decrease in precipitation during the monsoon season (Figure 4.2).

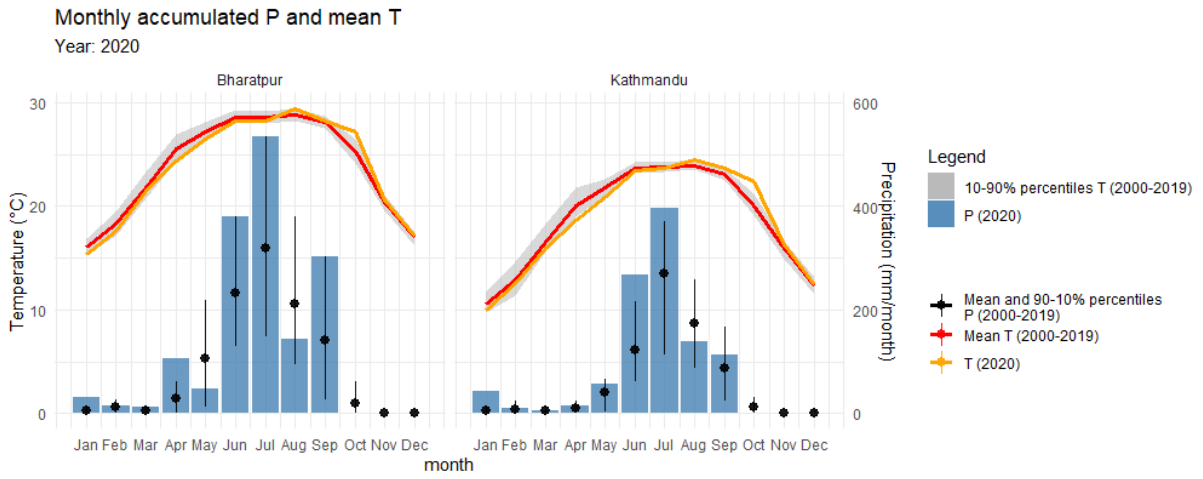

Figure 4.1 Monthly accumulated precipitation [mm/month] and mean temperature [°C] in 2020 at Bharatpur and Kathmandu compared to the long-term average (2000-2019) and the 10th and 90th percentiles.

Figure 4.2 Relative (top) and absolute (bottom) monthly anomalies of mean temperature (left) and accumulated precipitation (right) at Bharatpur and Kathmandu. All changes in precipitation above 100% are aggregated as a >100% positive change.

4.1.2 Growing degree days estimation

The effect of temperature on crop growth is reflected in the computation of a GDD model. The cumulative GDD has been estimated for three different crop growth seasons (Figure 4.3 & Appendix C.1). All different growth seasons have been estimated to sustain about three months until crop maturity has been reached. This is also displayed in the crop calendar of 2020 (Figure 4.4), where the timing of GDD threshold exceedance is converted to growth stages. The percentile range of the GDD for the 10% coldest and hottest years is very small for all crop growth seasons and locations, with a maximum difference of 200 GDD (°C) at the maturity stage of wheat at Kathmandu (Figure 4.3). This results in a delay or advance of about one week of crop maturity for years with exceptional temperature deviations. So, in general the growth stage occurrences solely based on daily temperatures are estimated to be consistent every year and independent of drought occurrence.

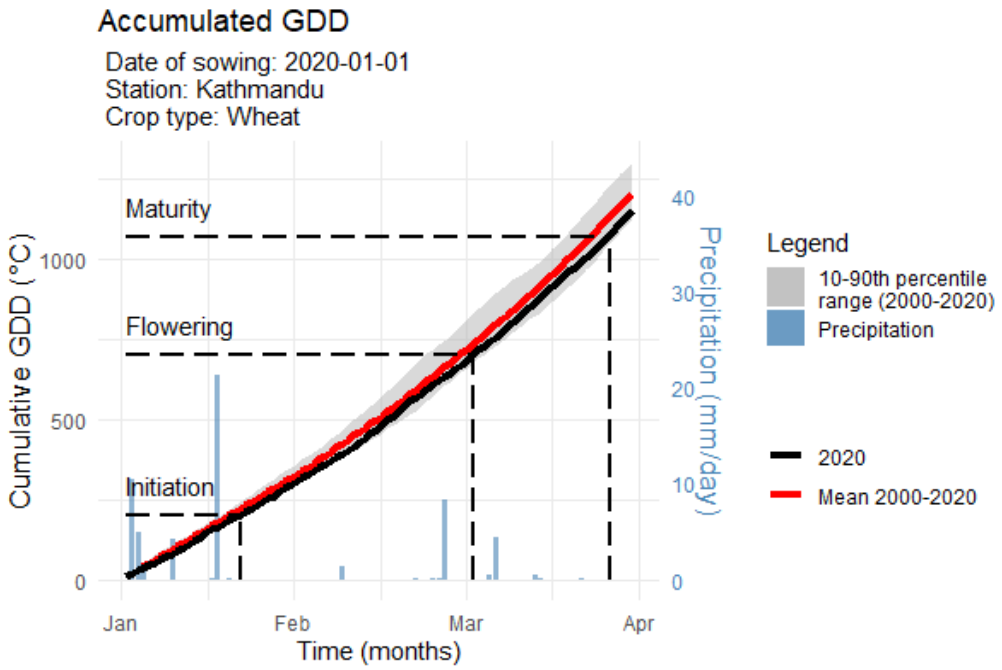

Figure 4.3 Cumulative growing degree days [°C] and corresponding growth stage thresholds for wheat crops at Kathmandu with a sowing date of 1 January 2020. Daily precipitation rates are indicated by the blue bars in mm/day.

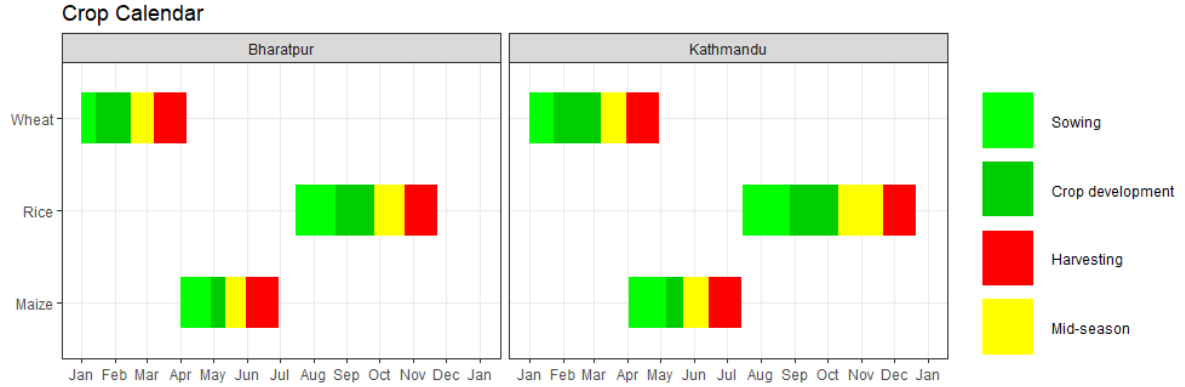

Figure 4.4 Crop calendar of growth stage occurrence for winter wheat, rice, and maize crops at Bharatpur and Kathmandu.

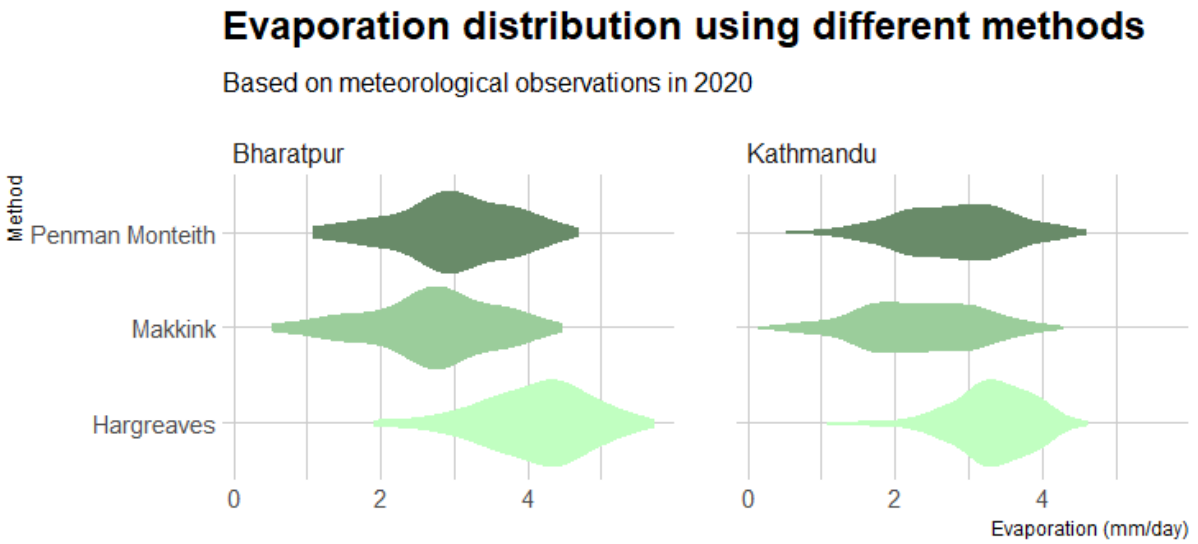

Figure 4.5 Distribution of evaporation [mm/day] computed using three different methods: Penman-Monteith, Makkink and Hargreaves. The computation is applied to measured station data for the time period available, so from January to December 2020 in Kathmandu and February to September 2020 in Bharatpur.

4.1.3 Cumulative climatic water balance

Figure 4.5 indicates the distributions of the potential evapotranspiration (ET_0) that is computed using three different methods: Penman-Monteith, Makkink and Hargreaves. The Penman-Monteith and Makkink ET_0 result in very similar distributions, whereas the distribution from the Hargreaves ET_0 is higher. The Penman-Monteith calculated ET_0 has a mean of 2.98 mm/day and the ET_0 calculated using Makkink has an average of 2.69 mm/day, while Hargreaves gives an average ET_0 of 4.09 mm/day at the station of Bharatpur. Thus, the method chosen for calculating evapotranspiration will have a considerable impact on the subsequent outcome of evaporation related computations, such as the climatic water balance (P-ET_0).

In Figure 4.6 this cumulative water balance is estimated over different crop seasons, that refer to the approximate growth seasons of wheat (January to May), maize (April to July), and rice (July to December) for Kathmandu and Bharatpur. The cumulative water balance is determined for 2020, the drought year of 2015, and the median, maximum, minimum, 10% highest and 10% lowest water balances observed between 2000 and 2020. For most growth seasons 2020 gives the highest cumulative water balance, indicating that 2020 has been the wettest year compared to the 20 years prior. When comparing the water balances of different growth seasons, it is also evident that the range in water balance at the end of the growth season is much smaller during the dry (winter) season than the (summer) monsoon season.

4.1.4 Crop specific cumulative climatic water balance

In Figure 4.7 the crop specific climatic water balance is considered for wheat, maize, and rice at Kathmandu and Bharatpur, where the water balance is calculated using crop evapotranspiration (P-ET_c). This alters the water balance such that it accounts for crop specific water use, thus indicating the actual water availability over a certain crop growth period. Similar to Figure 4.6, the crop specific water balance is obtained for 2020, the drought year of 2015, and the median, 10% wettest and 10% driest years over a period of 2000-2020. The water availability varies much over the growth seasons at the different stations and for the different crop types. Again, 2020 often results in an extremely high

water availability that accounts for the 10% wettest years. Even though 2020 indicates this relatively high water availability, during some crop seasons the occurrence of a negative water balance is inevitable, in particular during the winter season. Growth stages with the highest water demand, which is in this case the initial stage of rice crops, can, however, be compensated by a high rainfall input during the monsoon season.

As the 10^{th} to 90^{th} percentile range is broad and comprises both positive and negative water balances for many crop growth seasons, this graph can give an indication about when irrigation may be necessary. In the case of maize crop growth in Kathmandu, for example, the cumulative water balance in 2020 remains positive throughout almost the entire growth season, whereas for a median year irrigation may become necessary towards the end of the growth season.

Moreover, the crop specific cumulative water balance allows for monitoring of water availability during crop growth stages that are vulnerable to water stress. Rice is, for example, most sensitive to water stress at its flowering stage (Section 2.1.3) (Pandey & Thongbam, 2014), which occurs in October according to the GDD model. Figure 4.7 indicates that in 2020 during this stage no negative water balance occurred.

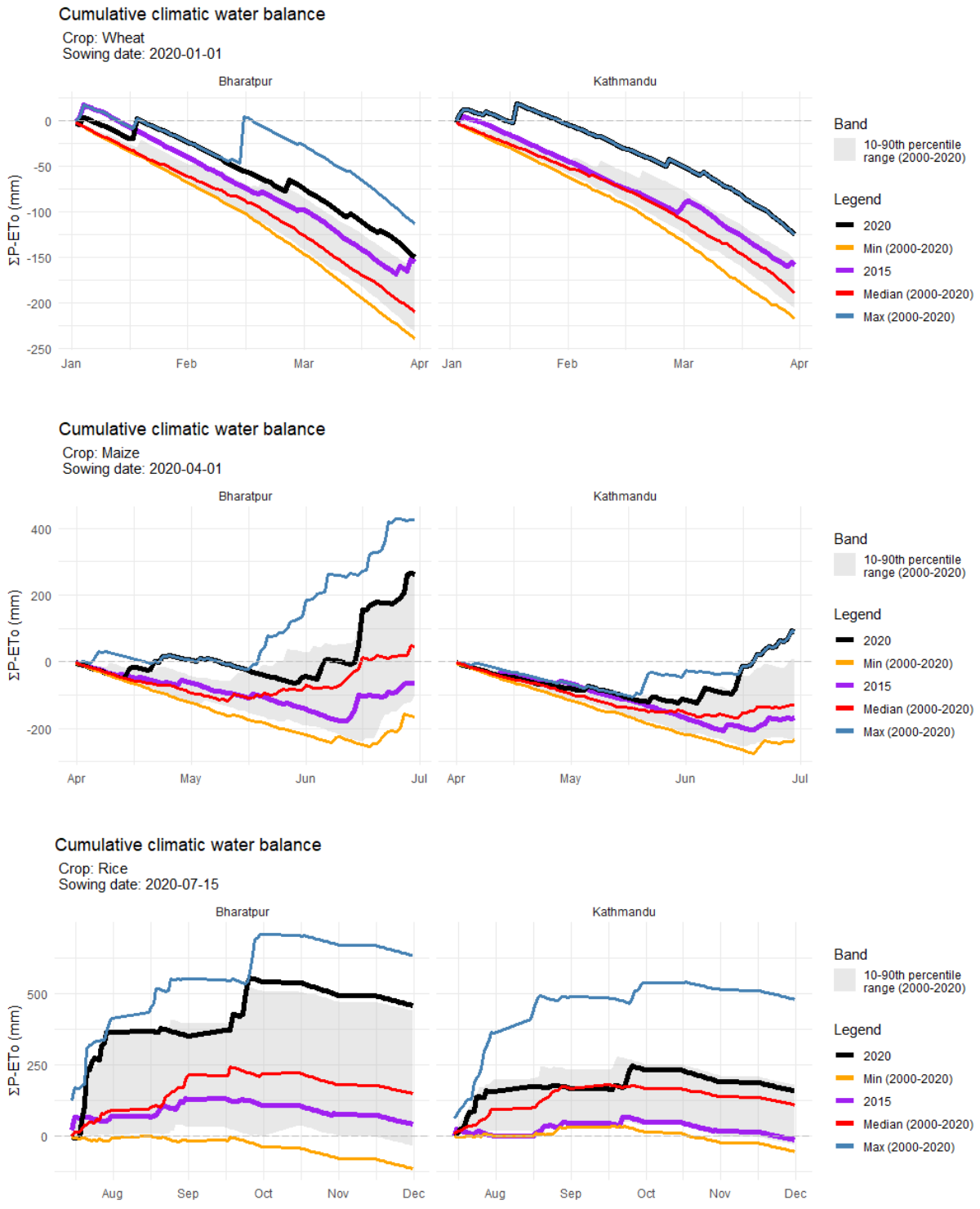

Figure 4.6 Cumulative climatic water balance [mm] in 2020, 2015 (drought year) and the long-term mean and percentiles over the crop growth season of wheat (top), maize (middle) and rice (bottom) at Bharatpur (left) and Kathmandu (right).

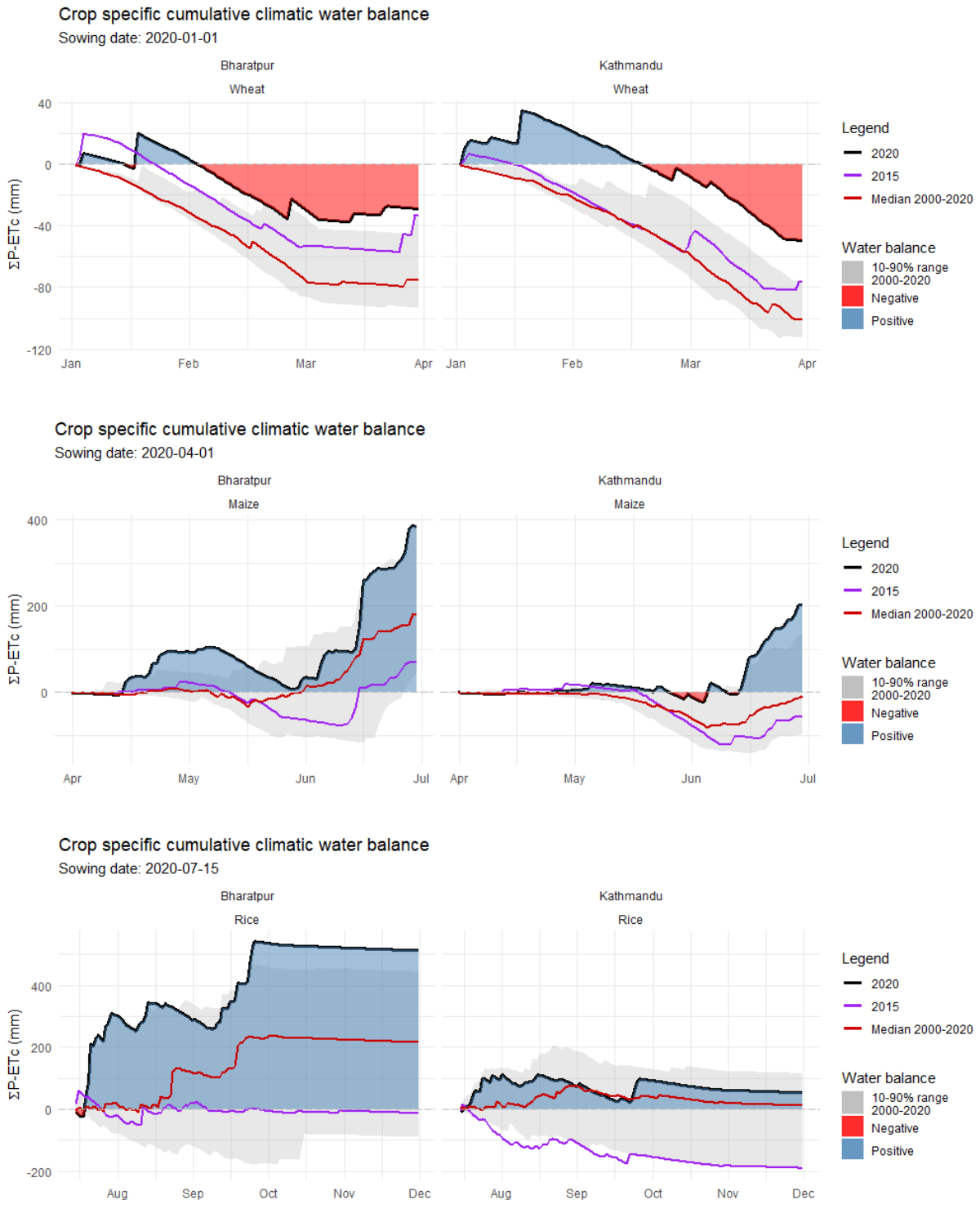

Figure 4.7 Crop specific climatic water balance [mm] in 2020, long-term mean and percentiles (2000-2020) for wheat (top), maize (middle) and rice (bottom) crops at Bharatpur (left) and Kathmandu (right).

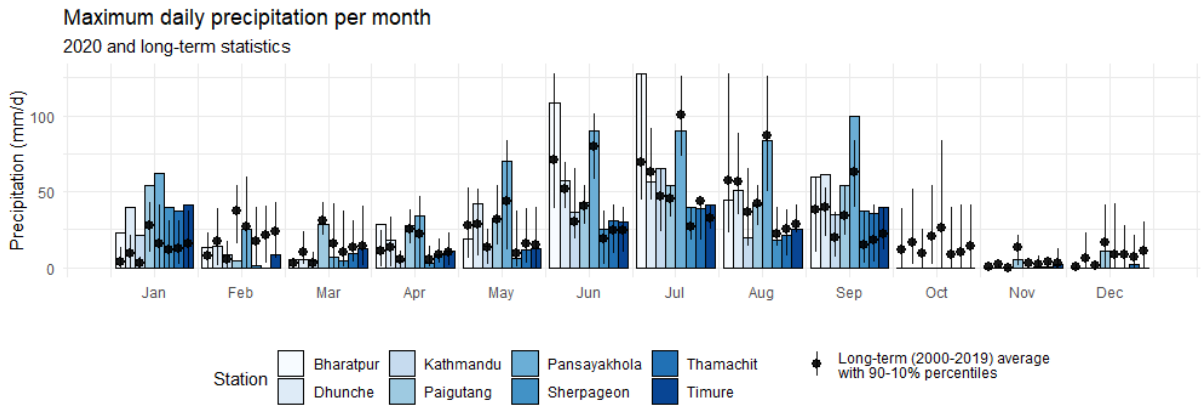

Figure 4.8 Maximum daily precipitation per month [mm/day] for all meteorological stations in 2020 compared to the long-term average and percentiles (2000-2020).

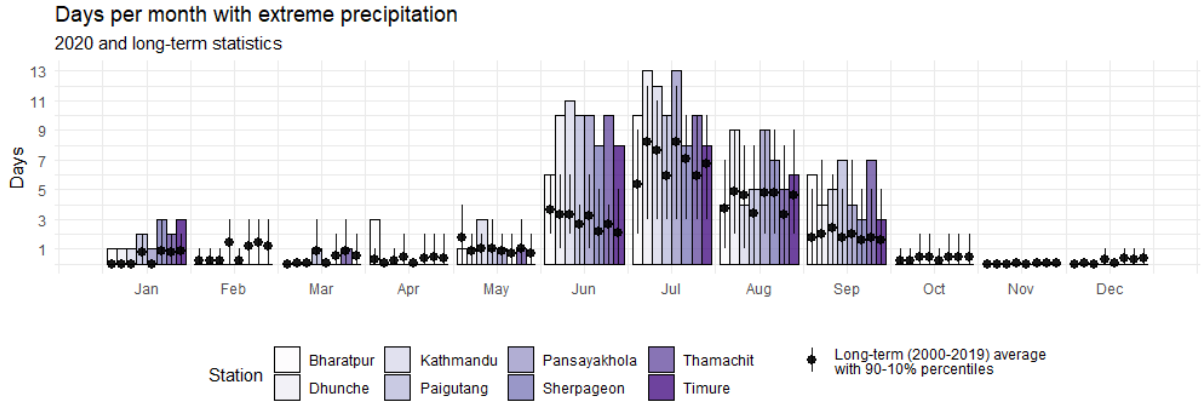

Figure 4.9 Days with extreme precipitation per month in 2020 compared to the long-term average and percentiles (2000-2020). Extreme precipitation occurs at exceedance of a long-term 95th percentile threshold.

4.2 Estimation of rainfall-triggered landslide potential

4.2.1 Occurrence of precipitation extremes

Extreme precipitation events are identified through estimation of the maximum daily precipitation rates [mm/day] (Figure 4.8) and the number of days with extreme daily precipitation rates (Figure 4.9) per month for all meteorological stations in the study area. Extreme precipitation is defined as a day on which the 5% highest daily precipitation rates obtained from long-term historical precipitation data are exceeded (Section 3.2.2.1).

The highest daily maximum precipitation rates occur during the monsoon season, although during other months the maximum monthly peak may also be high. The maximum daily precipitation peaks in 2020 were exceptionally high in January at all stations, whereas in October to December high precipitation peaks were lacking. The number of days with extreme precipitation were very high during the monsoon of 2020, reaching above the long-term average at most stations. During the dry season, the number of days with extremely high precipitation was very low.

4.2.2 Relation between landslides and precipitation

In Figure 4.11 the total precipitation per month [mm/month] is related to the number of landslides occurring at the corresponding month per meteorological station. All results show a positive trend, meaning that as the monthly precipitation increases, the total

number of landslides occurring in the near the meteorological station increases as well. To analyse this linear relation the R^2 has been estimated per station. The R^2 values indicate that the monthly precipitation is at some stations more related to landslide occurrence than at other locations. This relation is strongest for Pansayakhola (R^2 = 0.62; 21 landslides observed) and Kathmandu (R^2 = 0.40; 25 landslides observed), whereas the trend is unclear for stations where less landslides have occurred, such as Thamachit (R^2 = 0.07; 2 landslides observed).

At a higher temporal resolution, the maximum daily precipitation intensity is determined [mm/h] and linked to days with landslide occurrence near Kathmandu (Figure 4.12) and Bharatpur (Appendix C.2). As visualised, not all days with peak intensities are associated with the occurrence of a landslide. Figure 4.10a indicates the percentage of days with a landslide occurrence on which a precipitation event was measured. It shows that on most days (94.5%) that a landslide occurred from 2017 to 2020, the daily precipitation was larger than zero, meaning that on almost all landsliding days precipitation events occurred. This and the positive trend between monthly precipitation and landslide frequency imply that precipitation obtained from the downscaled dataset in this study has potential as a proxy for identification of landslide risk in the study area.

When analysing the intensity and duration of rainfall events prior to slope failures, the duration and mean intensity of these events are often relatively short according to the downscaled reanalysis dataset (Figure 4.10b). The majority of rainfall events remain below an intensity of 5 mm/h and a duration of 10 hours. So, when an event has a very low duration, the intensity is more likely to be low as well, and vice versa. This implies that precipitation events do not necessarily have a very high duration or intensity when triggering a landslide.

(a)

Station	**Days with precipitation [%]**
Kathmandu	90.3
Bharatpur	86.6
Pansayakhola	91.7
Sherpagaon	100
Timure	100
Dhunche	100
Mean	94.5

(b)

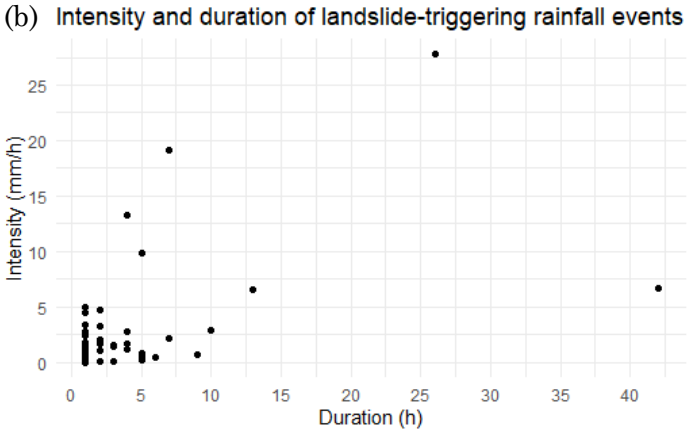

Figure 4.10 (a) Percentage of days with a landslide event on which precipitation was measured and (b) the intensity and duration of rainfall events that triggered landslides in Kathmandu and Bharatpur between 2017 and 2020.

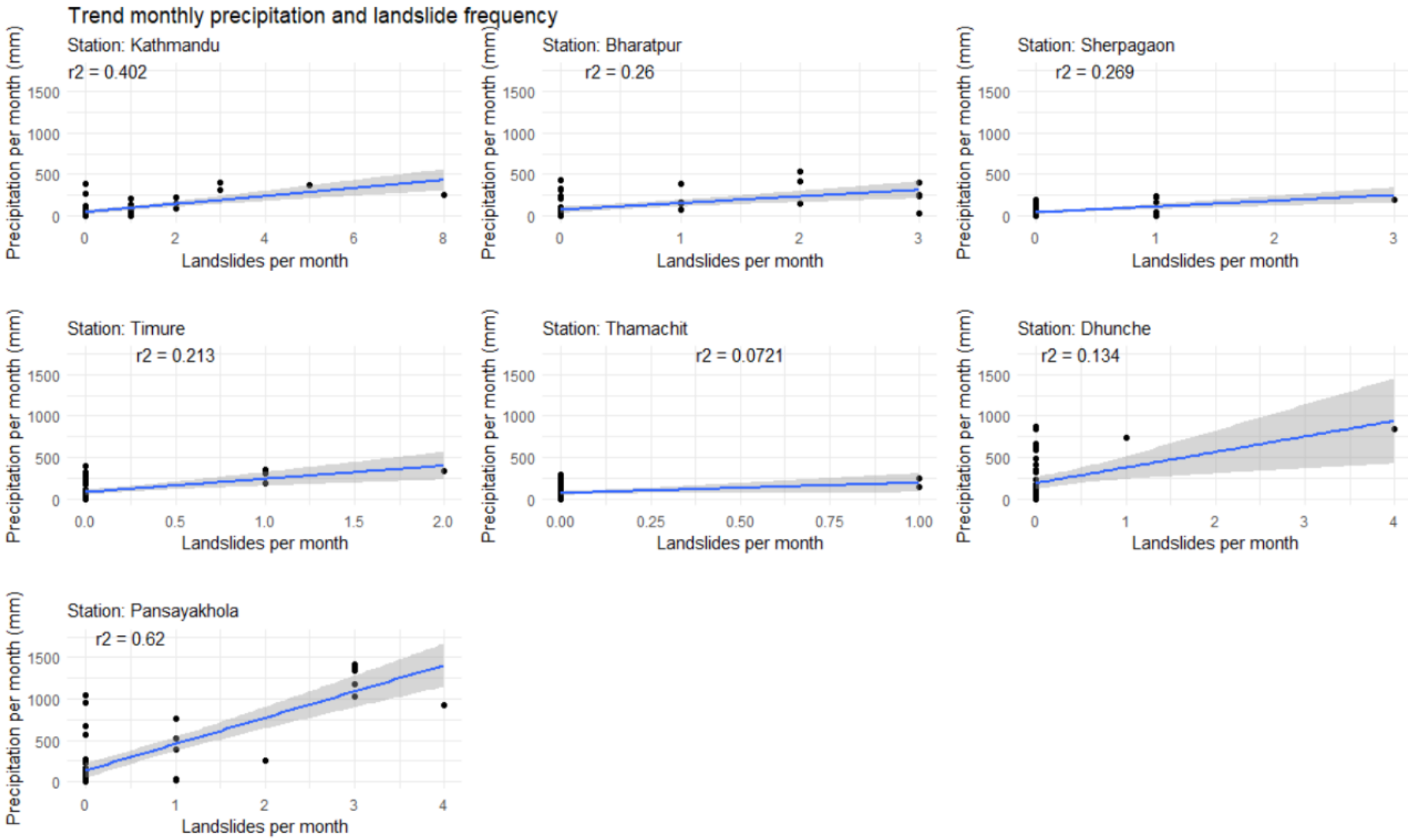

Figure 4.11 Adjusted R^2 for the relation between monthly number of landslides (2017-2020) and precipitation [mm/month] per station.

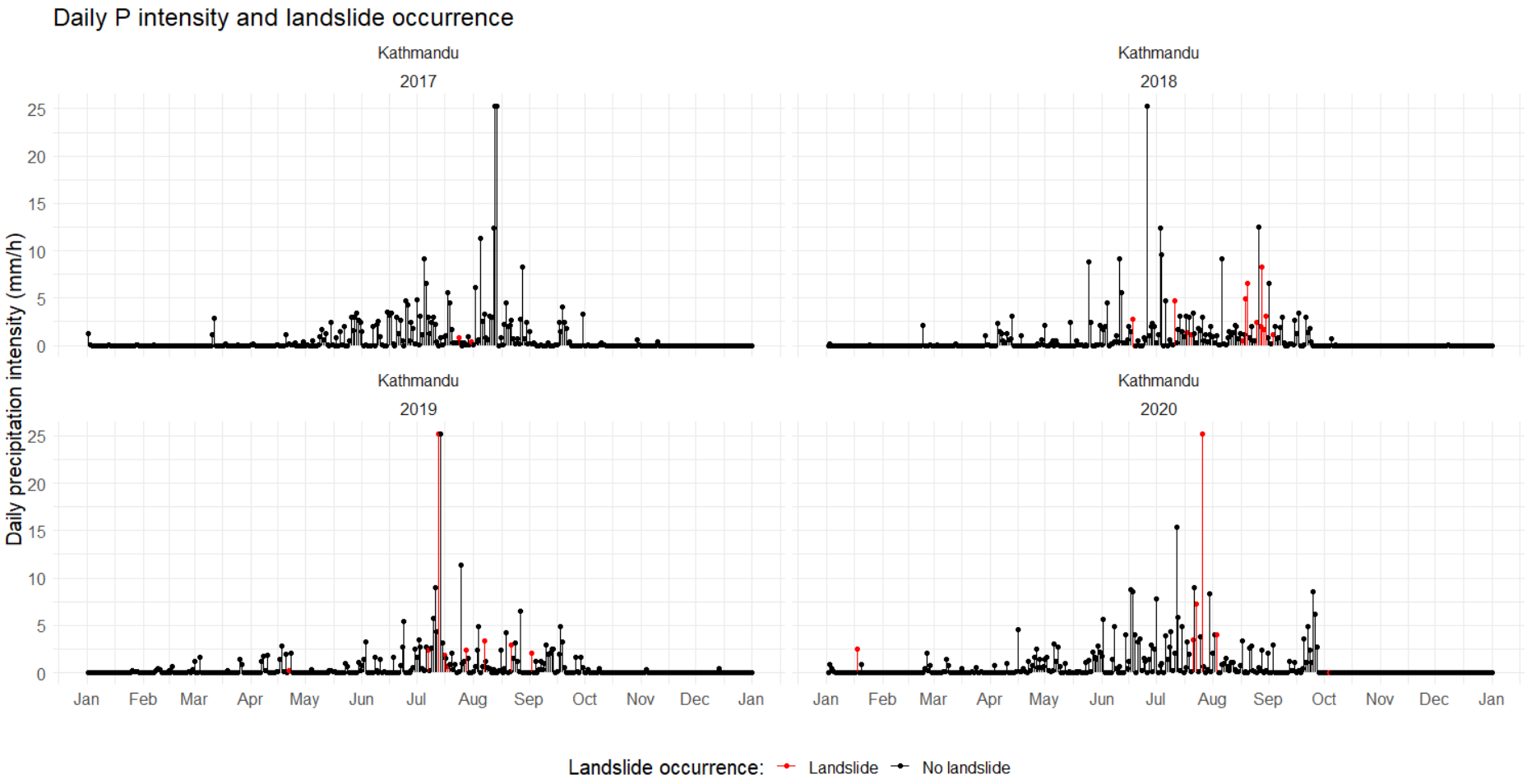

Figure 4.12 Maximum daily precipitation intensity [mm/h] and landslide occurrence (red) in proximity to the Kathmandu station from 2017 to 2020.

4.2.3 ARI landslide potential

In this study the Antecedent Rainfall Index (ARI) is used to estimate rainfall-induced landslide risk in proximity to the meteorological stations in the Trishuli catchment. The days that landslide risk is increased due to an extremely high ARI value from 2017 to 2020 at, for example, Kathmandu are displayed in a landslide risk calendar (Figure 4.13). The landslide risk calendars for the other stations are available in Appendix C.3, and Figure 4.14 indicates daily landslide risk map. A great majority of the days with high landslide risk are estimated to occur in June to August, so during the monsoon season. Kathmandu has, compared to the other stations, the highest amount days with landslide risk predicted, while at Dhunche the least number of landslides are estimated to occur from 2017 to 2020.

The performance of the ARI landslide risk is evaluated by comparing it to the landslide inventory of Nepal Disaster Risk Reduction Portal (Appendix C.4). Per station the historical landslides are selected that are in closest proximity to the respective station. The performance metrics and indicators calculated for all stations are presented in Table 4.1. The amount of estimated true positives (TP) is for all stations lower than the number of false negatives (FN), meaning that the TP_{rate} is low (≤ 0.5) and the majority of the landsliding events are not identified by the ARI proxy. The Thamachit station has the highest performance for this classifier, missing 50% of the landslide occurrences. The number of true negatives (TN) is high for all stations compared to the number of false positives (FP), meaning that the TN_{rate} is high (~0.95), and the method is able to correctly estimate most of the days without landslide events. The precision is overall very low (0.01-0.13), which indicates that the rate of false alarms is high. The accuracy is, however, high (~ 0.94), meaning that the predictions are in general correct for more than 90% of the time, which can mainly be attributed to the high amount of correctly estimated days without slope failure.

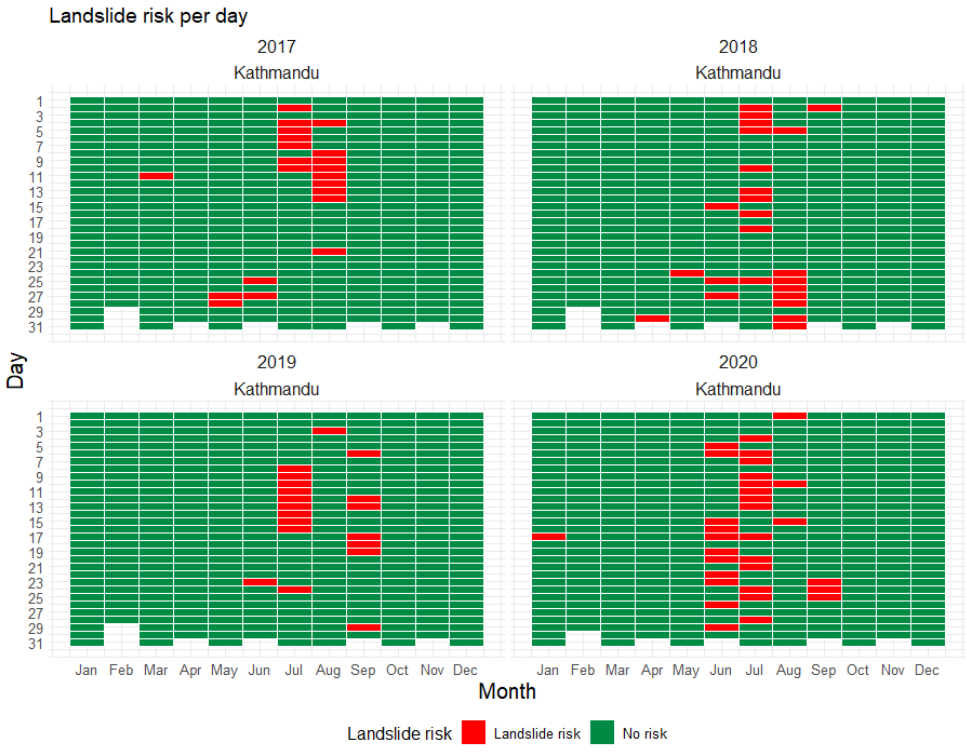

Figure 4.13 Daily landslide risk (2017-2020) in Kathmandu as estimated by the ARI. Days in red indicate a high risk of rainfall-induced landslide occurrence while days in green imply no landslide risk.

When the spatial match of landslides is disregarded, so all 124 landslides that have been registered between 2017 and 2020 in Central Nepal, regardless of their proximity to a station, are compared to the ARI landslide risk prediction, the values of the performance metrices change slightly (Table 4.2). This mainly has implications for the TP_{rate}, which decreases for most stations (mean change of -7%), and the precision that increases at all stations (mean change of +24%). Since the TP_{rate} is the most important classifier, indicating to what extent alarms are missed, a decrease in the TP_{rate} suggests that a more exact spatial match between the location of precipitation measurement and landslide occurrence improves ARI landslide detection.

On a lower temporal resolution with landslide risk estimation on a weekly scale, the values of the performance indicators change as well (Table 4.2 & Figure 4.15). The TP_{rate} is positively affected for most stations (mean change of +17%) as well as the precision (mean change of +13%), so more landslide events are correctly predicted. The highest increase in landslide prediction is found at Bharatpur, where the correct detection increased by 37%. The prediction of weeks without landslides, however, decreases (mean change of -11%), as well as the overall true predictions (mean change of -12%).

Table 4.1 Performance classifiers for landslide risk estimated by the ARI with a spatially matched landslide inventory on daily scale ($Inv_{spat,d}$).

Station	TN	FN	TP	FP	TPrate	TNrate	Precision	Accuracy
Bharatpur	1357	17	5	82	0.227	0.943	0.058	0.932
Dhunche	1389	3	2	67	0.400	0.954	0.029	0.952
Kathmandu	1346	19	12	84	0.387	0.941	0.125	0.930
Pansayakhola	1355	23	6	77	0.207	0.946	0.072	0.932
Sherpagaon	1382	9	3	67	0.250	0.954	0.043	0.948
Thamachit	1365	1	1	94	0.500	0.936	0.011	0.935
Timure	1385	4	1	71	0.200	0.951	0.014	0.949
Mean	1368	11	4	77	0.310	0.950	0.050	0.940

Table 4.2 Difference between performance classifiers for a landslide inventory that is not spatially matched and the spatially matched landslide inventory (left; $Inv_{total,d}$-$Inv_{spat,d}$), and the difference between performance classifiers of a landslide inventory on weekly scale and a landslide inventory on daily scale (right; $Inv_{spat,w}$-$Inv_{spat,d}$). Values in red indicate a negative change and in green a positive change of the classifier.

Station	TPrate	TNrate	Precision	Accuracy	TPrate	TNrate	Precision	Accuracy
Bharatpur	-0.006	0.009	0.184	-0.028	0.373	-0.112	0.216	-0.123
Dhunche	-0.179	0.002	0.275	-0.036	-0.150	-0.086	0.007	-0.096
Kathmandu	-0.071	0.011	0.187	-0.020	0.158	-0.096	0.168	-0.117
Pansayakhola	0.035	0.010	0.205	-0.022	0.353	-0.055	0.340	-0.080
Sherpagaon	-0.018	0.011	0.271	-0.031	0.250	-0.111	0.119	-0.125
Thamachit	-0.247	0.012	0.243	-0.032	0.000	-0.158	0.011	-0.160
Timure	0.032	0.012	0.292	-0.033	0.200	-0.127	0.039	-0.136
Mean	-0.065	0.010	0.237	-0.029	0.169	-0.106	0.128	-0.120

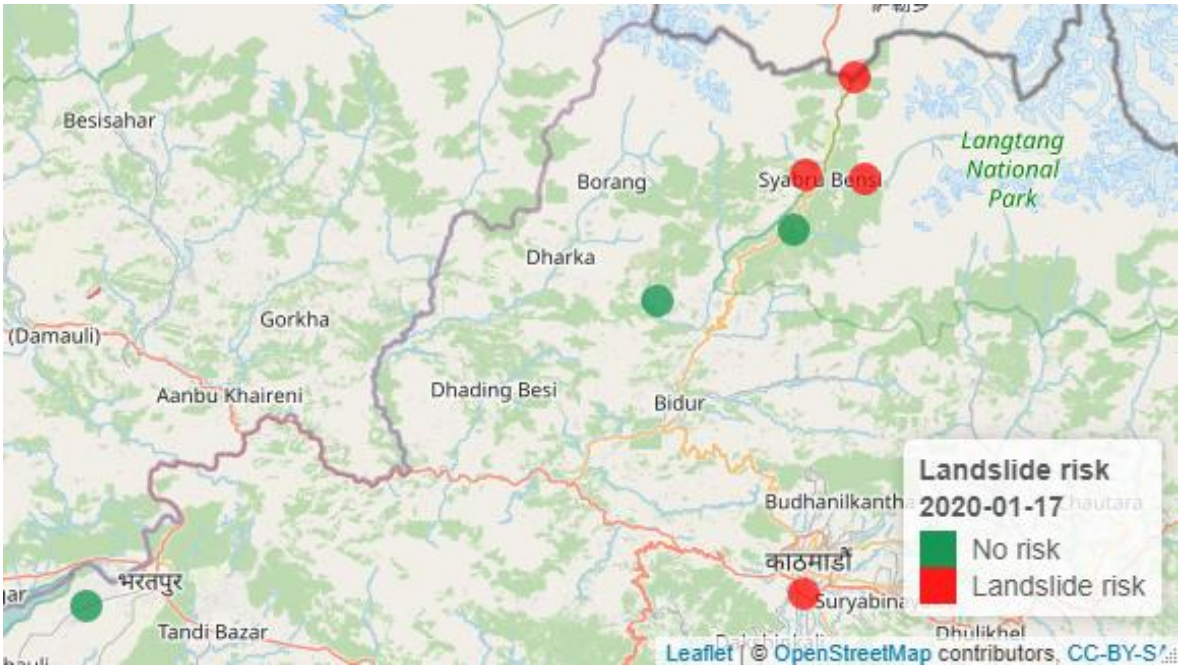

Figure 4.14 Daily rainfall-induced landslide risk map at Timure, Kathmandu, Bharatpur, Sherpagaon, Thamachit, Dhunche and Pansayakhola based on the exceedance of ARI threshold.

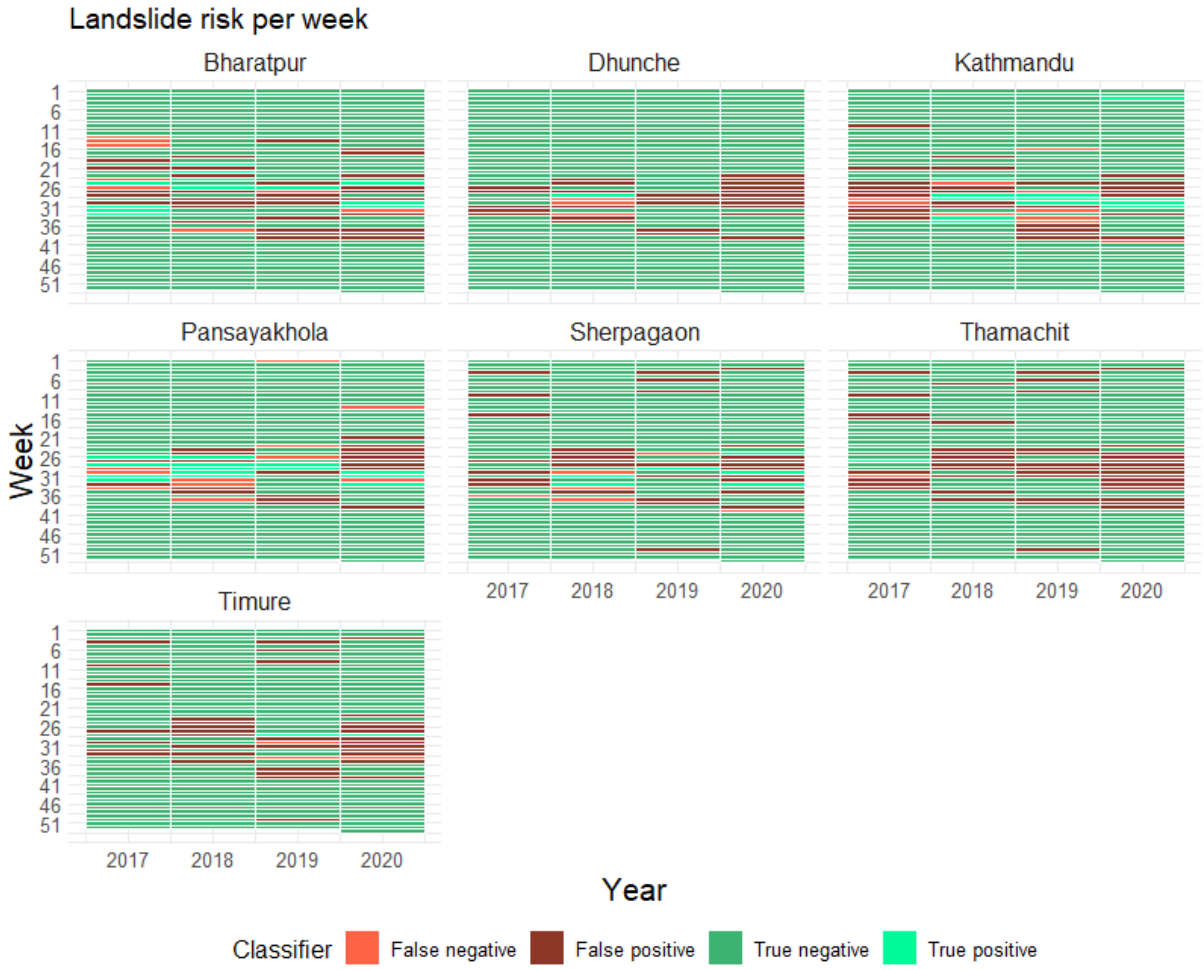

Figure 4.15 Performance of ARI predicted landslide potential on weekly scale compared to the landslide inventory of 2017-2020 (DRR Nepal).

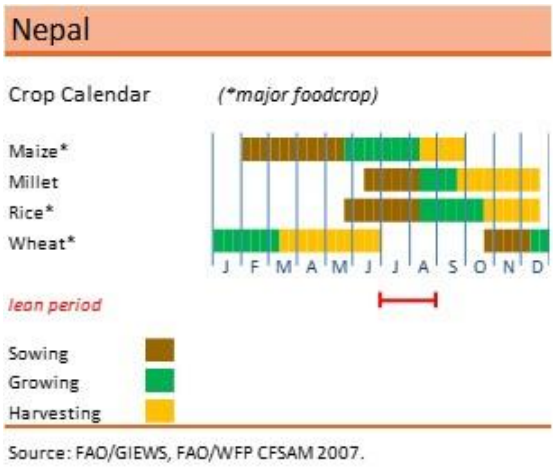

Figure 5.1 Crop calendar of the major food crops in Nepal (FAO, 2021).

5. Discussion

5.1 Validation

5.1.1 GDD and growth stage occurrence

The crop phenology is mainly dependent on the empirical values of the GDD thresholds. These have been obtained from previous work in Nepal (Amgain, 2011, 2013; Karki & Amgain, 2015). In those studies, the GDD thresholds are estimated for different sowing dates and cultivars. The subsequent variation in GDD thresholds at certain conditions can be significant, e.g. delayed planting of maize can cause a decrease of 400 degree days at the physiological maturity threshold. These variations in GDD thresholds are, however, neglected for this study, and simply one mean estimation per crop type is used (Table 3.2). Also, the lower and upper threshold of the GDD calculation (T_{base} and T_{upper}) are assumed or disregarded in this study due to lack of data. Nevertheless, the growth stage lengths (Figure 4.4) are very comparable to those indicated in Figure 5.1, which is an average crop calendar of the major crops in Nepal (FAO, 2021). Therefore, the GDD model generated by the downscaled meteorological dataset has potential for estimating plant phenology, regardless of some specific empirical inputs. Since the accumulated GDD has been relatively similar over last decades (Figure 4.3 & Appendix C.1), delays in harvesting are not expected to be caused by variations in temperature. They are more likely due timing of monsoon onset or other factors contributing to crop stress, such as diseases, soil salinity, low soil fertility, water shortage or waterlogging (Allen et al., 1998).

5.1.2 Makkink, Hargreaves and Penman-Monteith ET_0

The Penman-Monteith equation is often considered as the most accurate method for estimating evapotranspiration, since the method is physically-based and more robust as it includes all parameters that govern the latent heat flux (evapotranspiration) (Allen et al., 1998; Beguería et al., 2014). In general, the FAO-56 Penman-Monteith method is considered as the standard method to compute ET_0 from meteorological data, although its superiority has been criticized and field measurements of ET_0 remain the most reliable (Liu et al., 2017).

As not all meteorological variables necessary to calculate ET_0 through Penman-Monteith are available in the downscaled dataset, the methodology that remains closest to Penman-Monteith is selected for further calculations involving ET_0. This is the case for the Makkink method rather than Hargreaves (Figure 4.5). This is likely due to the

parameterization of Makkink that involves both temperature and solar radiation measurements. Makkink also accounts for other climatic parameters derived from the meteorological data, such as the saturation vapour pressure, the psychometric constant and the heat of vaporization. Hargreaves, on the other hand, only involves temperature measurements combined with some empirical constants (Appendix B). Although the computation of Makkink requires more effort and input data, its outcomes are thus more realistic than Hargreaves. Therefore, Makkink is the recommended method when computing ET_0 if computation of Penman-Monteith is not possible.

5.1.3 Climatic water balance and crop specific water demand

The monsoon season of 2020 is estimated in this study as an extremely wet monsoon compared to the past 20 years. The year also stood out as a wet year while analysing the water balances of the different crop growth seasons in 2020 (Section 4.1.3 & 4.1.4). This is in agreement with observations of the 2020 monsoon summer in Nepal from other sources (Department of Hydrology and Meteorology, 2021; FAO, 2021). The Nepalese Department of Hydrology and Meteorology reported eight station with a record-breaking total precipitation during the monsoon season of 2020. The absolute value of measured precipitation in Kathmandu during the 2020 monsoon season was, however, somewhat higher (1200 mm; Figure 5.2a) than the accumulated precipitation obtained from the downscaled ERA5 dataset over this season (918 mm; Figure 5.2b) (Department of Hydrology and Meteorology, 2020). This suggests that there is a possible underestimation in monsoon precipitation of the downscaled ERA5 data, although stations are not at the exact same locations.

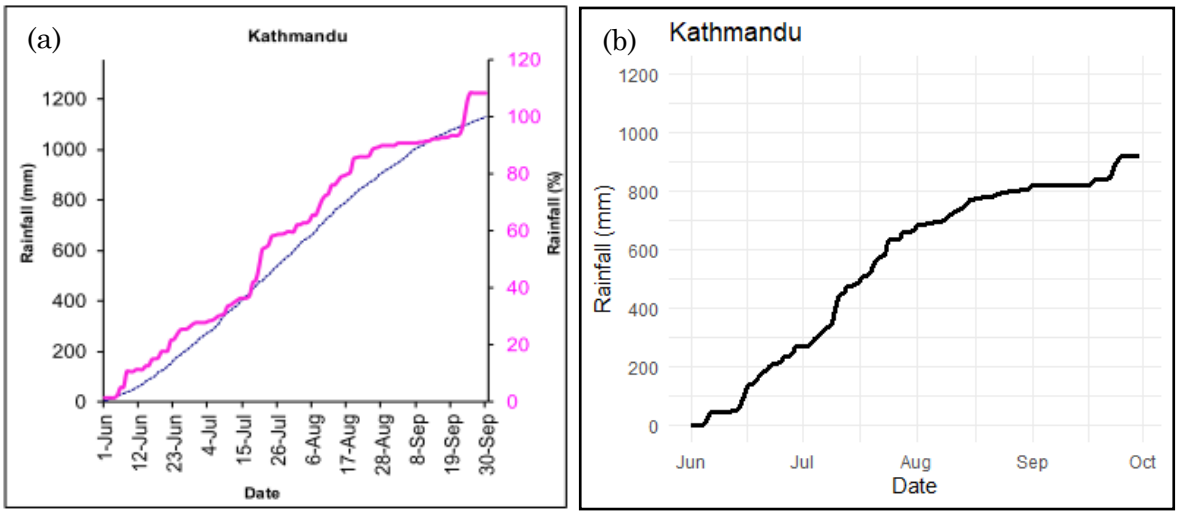

Figure 5.2 (a) Accumulated monsoon rainfall (pink line; June-September 2020) at Kathmandu Airport monitored by the Nepalese Department of Hydrology and Meteorology (2020). The blue dotted line indicates daily accumulated mean precipitation as estimated over 30 years (1981-2010) and the second y-axis on the right side (pink) gives the percentage of this average accumulated monsoon rainfall. (b) Accumulated monsoon rainfall (June-September 2020) at the REAMO Kathmandu station from the downscaled reanalysis data.

When comparing the calculated accumulated evapotranspiration rates (ET_c) of each crop season to evapotranspiration measured by lysimeters in a field study (ET_a), deviations have been found as well (Bhandari, 2011, 2012; Bhandari & Kayastha, 2012). These deviations can be found in Table 5.1, with Bhairahawa as the location of the lysimeter, which is located roughly 114 km west of Bharatpur and 207 km west of Kathmandu. The largest deviation occurs during the rice crop season, where the measured

evapotranspiration is almost three times as high as the computed ET_c. This emphasizes that the Makkink ET_0 model is not a perfect representation of reality, as would be the case for any other ET_0 model (Liu et al., 2017). To enhance the performance of Makkink, it is suggested to locally calibrate the coefficient c (Eq. 5) to meteorological variables (Liu et al., 2017). It should, however, be considered that the lysimeter was not placed at the exact same location as the stations. Moreover, ET_c assumes that the crops are grown under perfect conditions, meaning that they are disease-free, well-fertilized, and with optimum soil and water conditions, so that they can achieve full production (Allen et al., 1998). This scenario is unrealistic and could, therefore, possibly explain the large deviations between ET_c and ET_a.

Table 5.1 Accumulated ET_a measured by a lysimeter at Bhairahawa and accumulated ET_c calculated using Makkink at Bharatpur and Kathmandu during their growth seasons in 2010 and 2011.

Crop	**Growth season**	**Cumulative ET_c** (Bharatpur) [mm]	**Cumulative ET_c** (Kathmandu) [mm]	**Cumulative ET_a** (Bhairahawa)[a] [mm]
Wheat	Jan-May (2011)	101	125	238
Maize	Apr-Jul (2011)	162	164	487
Rice	Jul-Dec (2010)	336	390	997

[a] Obtained from Bhandari (2011, 2012) for wheat and maize, and Bhandari & Kayastha (2012) for rice.

5.1.4 ID curve

When comparing the intensity and duration of landslide-triggering rainfall events to the intensity-duration (ID) curve threshold obtained from Dahal and Hasegawa (2008) in Nepal Himalaya (Figure 5.3), only three precipitation events associated with landsliding exceed this threshold. So, the ID threshold only accounts for 5.7% of the total amount of landslides in the study area. Therefore, this ID curve does not represent the relation between rainfall characteristics and landslide occurrence correctly for the downscaled data in this study area. A probable reason for this is that the ID curve does not include antecedent rainfall conditions, while these are crucial when relating landslides to rainfall (Section 2.2.1). Moreover, the threshold is very static and generalized over the entire Nepalese Himalaya, whereas the variation in climatic and physiographical conditions is very high in Nepal (Section 2.3). It should also be considered that limitations of the landslide inventory may have affected the accuracy of the ID curve for detecting landslide events. It is, for example, unknown at what hour the landslide occurred, so the assumption is made that a landslide occurs at the hour of peak rainfall intensity. Also, it is unknown to what extent the landslide inventory represents landslides that are solely triggered by precipitation. Dahal and Hasegawa (2008) filtered many landslides from their inventory, using only 193 out of 677 reported landslides, which suggests that particular requirements must be met before a landslide is associated with rainfall data.

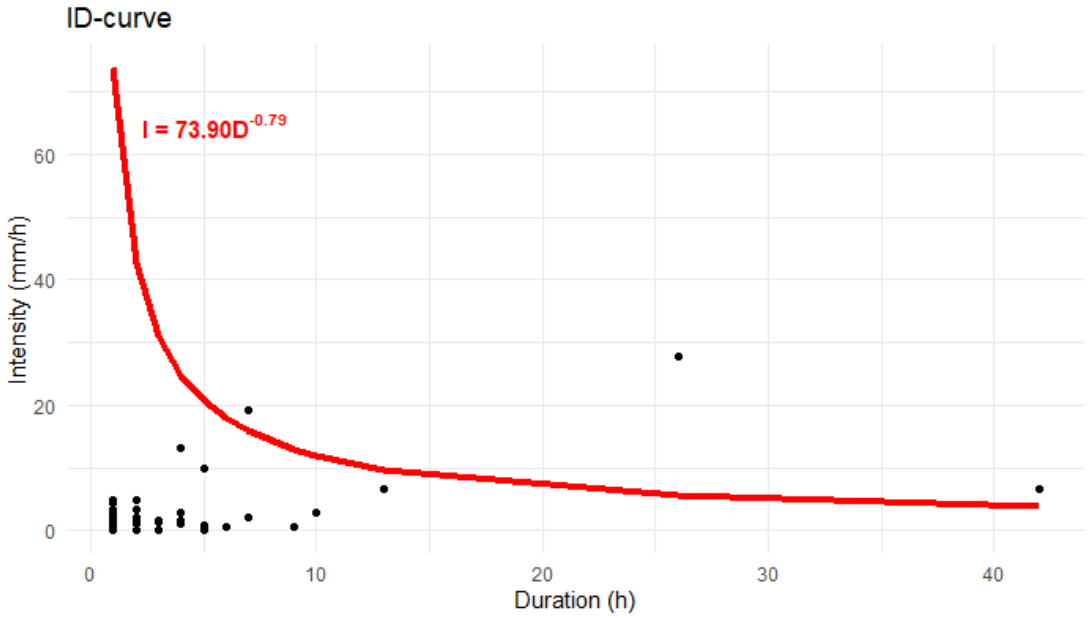

Figure 5.3 Intensity-duration (ID) curve threshold for landslides in the Nepalese Himalaya (red) as estimated by Dahal & Hasegawa (2008), and the intensity and duration of rainfall events coinciding with 53 landslide occurrences near Bharatpur and Kathmandu between 2017 and 2020.

5.1.5 Performance of ARI landslide estimation

The ARI landslide monitor predicts the highest landslide frequency during the monsoon season (Jul-Aug), which is in agreement with the occurrence of reported landslides (Department of Hydrology and Meteorology, 2021; Government of Nepal, 2021). The largest challenge for the development of a landslide monitoring system is that the number of events where the system fails to alert landsliding (FN) should be minimized, while also avoiding the occurrence of too many false alerts (FP). It is, however, more desirable that all landsliding events are noticed, rather than having the lowest number of false alarms. This implies that the TP_{rate} is the most important indicator when evaluating the performance of the ARI threshold. As the TP_{rate} improves when landslide events are spatially matched to the different stations, it is recommended to execute spatial modelling of precipitation and subsequent ARI values to obtain an improved spatial match for local patterns in precipitation and landslide occurrence.

Figure C.4 of Appendix C indicates that false negatives often occur at the end of the monsoon period (Aug-Sep). This could imply that prolonged antecedent conditions affect landsliding, and that towards the end of the monsoon period the threshold value of precipitation triggering a landslide is lower. Moreover, false negatives occasionally occur one day prior, between or after days with false positives. The ARI methodology is, thus, very close to accurate prediction but often one day off, which might be due to other landslide triggering and predisposing factors (Section 2.2). When decreasing the temporal resolution of the ARI to a weekly scale, the TP_{rate} improves. So, considering a broader temporal window increases the overall probability of landslide detection.

The performance classifiers that are obtained by evaluating the ARI method with the DRR landslide inventory can be compared to the performance indicators of other methods for detecting landslides. Table 5.2 gives an overview of the mean skill score obtained in this study, and those obtained from other studies and methodologies. Overall, the TP_{rate} of this study is relatively low compared to these more comprehensive studies. Kirschbaum &

Stanley (2018) used a similar methodology, the difference is that they used remotely sensed precipitation input data and their landslide inventory was more extensive, covering over 7000 landslides in Nepal, resulting in a much higher TP_{rate}. The study conducted by Mirus, Becker, et al. (2018) shows that in situ precipitation combined with soil moisture measurements gives even better predictions of landslide occurrence. Such a network of soil moisture measurements would, however, be rather expensive and require high maintenance to implement throughout the entire Trishuli catchment. The TRIGRS model, which is a physically-based model predicting landslide occurrence, gives a more comparable TP_{rate}, meaning that a TP_{rate} does not necessarily have to be very high for an acceptable performance. A very high TP rate has recently been obtained by Liu et al. (2021), where different machine learning techniques were used to predict landslide occurrence, so there might be potential in using such techniques alternatively.

5.2 Accuracy of datasets

5.2.1 Limitations of landslide inventory

The high rate of false positives (Section 4.2.3 & Appendix C.4) may be partially attributed to limitations of the landslide inventory. Also, the analysis of a relation between landslides and precipitation (Section 4.2.2) is affected by the size of the landslide inventory. The landslide inventory is in general not very large and only considers landslides that are reported by the Nepalese police, thus that are located in populated and accessible areas. Other studies often use widescale remote sensing techniques (Ambrosi et al., 2018; Dahal, 2014; Muñoz-Torrero Manchado et al., 2021) that are not limited to a landslides' accessibility or are based on an extensive media review (Dahal et al., 2014; Petley et al., 2007). These studies, thus, obtain a more complete landslide inventory.

Also, the landslide inventory does not differentiate between causal factors. Subsequently, it is unknown to what extent the landslide inventory represents rainfall-induced landslides. In any case, the landslide inventory is obtained for a period well after the occurrence of the devastating 2015 Gorkha earthquake that triggered at least 25,000 landslides in Central Nepal (Roback et al., 2018). It is, however, plausible that some other small earthquake events triggered landslides between 2017 to 2020, or that other causal factors were involved (Figure 2.2). Rosser et al. (2021) indicated that the landslide occurrence is still elevated since the occurrence of the Gorkha earthquake. Therefore, landslide detection by the ARI method should be considered as an increase in landslide risk. When the ARI landslide risk is linked to a regional susceptibility map, the potential of the method to indicate locations that are actually prone to landsliding will increase.

Table 5.2 Mean of the performance classifiers for all stations in this study (ARI), and classifiers obtained from other studies using different methods to detect landslide occurrence with the location of the study areas.

Method	TP_{rate}	Location	Reference
ARI	0.31	Central Nepal	This study
ARI	0.39-0.60	Nepal	Kirschbaum & Stanley, 2018
Antecedent saturation	0.77	USA	Mirus, Becker, et al., 2018
TRIGRS (physical model)	0.35-0.50	Indian Himalaya	Dikshit et al., 2019
Remote sensing (hindcast)	0.64-0.94	West Nepal	Muñoz-Torrero Manchado et al., 2021
Machine learning techniques	0.95	Norway	Liu et al., 2021

5.2.2 Accuracy of downscaled dataset

In this study all results are generated by meteorological variables obtained from the downscaled ERA5 dataset, meaning that no actual observations have been used in this study. This has consequences for the accuracy of all results and the subsequent interpretation. The downscaling of the ERA5 data compensates for biases in reanalysis data to some extent, some differences, however, remain.

Firstly, the variability of the downscaled ERA5 dataset is very dependent on the variability of data from the calibration period. If the calibration period is short, the extent of the extreme values will be limited to those observed within that period. Since the calibration periods are short for especially some of the REAMO stations, this underestimation of extreme values is highly likely to occur in the downscaled datasets of these stations. Consequently, the variability in climatic variables may be underestimated, which has impact on the applications, especially those with regards to drought monitoring due to the importance of absolute values. This could also be a possible explanation for the differences between the cumulative precipitation and evapotranspiration obtained in this study compared to those from field observations (Section 5.1.3).

Secondly, quantile mapping does not correct for the temporal shift of meteorological extremes that is present when comparing grid box observations to local observations. This has mostly implications for the ARI landslide risk assessment since timing of extreme precipitation events is essential for landslide risk estimation. The temporal shift in precipitation extremes is plausibly affecting the performance of the ARI method, increasing the number of false negatives and false positives. If the ARI would be applied to in situ observations, it is expected that landslide detection will improve.

Nevertheless, in this study it is of greater importance that the input dataset consists of a continuous and extensive timeseries rather than a timeseries with high accuracy since the main aim of this study is to find the potential of generating accessible monitoring methodologies from meteorological variables. Now that this has been achieved, the methodology developed in this study can be applied to real-time observations of the meteorological stations which will discard all inaccuracies induced by the usage of downscaled data.

5.3 Future recommendations

This study shows that relatively simple methods allow for quite accurate results for estimation of drought or landslide occurrence. The simplicity of the methodology also increases the likelihood of the implementation of accessible and understandable visualisations due to the reduced amount of effort. The most important applications for drought and landslide potential that are visualised in this study are the agricultural water availability per crop season (Figure 4.7) and ARI landslide potential (Figure 4.13 & Figure 4.14), respectively. While other visualisations, such as Figures 4.1, 4.2, 4.4, 4.8, 4.9 and 4.12 can provide additional information on hazard awareness. The R code that generates these visualisations can be applied to formatting online apps through, for example, RStudio's Shiny framework. This package allows for showcasing of plots or maps that are manipulatable by specified input variables, resulting in interactive web applications. These inputs could, for example, represent a certain data range, such as a particular year or crop season, or parameters, such as crop type and corresponding GDD thresholds.

For now, the methodology is applied to the downscaled ERA5 dataset. Section 5.2.2 remarks the necessity for using real-time meteorological observations when available, to

remove some biases in the results caused by downscaled data. The applications would become even more effective when applied to forecasting data. By using predictions of daily precipitation, temperature, and solar radiation, the web applications could operate as an early warning system for landslides or precipitation deficits. This would then allow for awareness and mitigation for potential occurrence of climatological hazards useful to local communities.

The high topographic variability and consequent high spatial variability in climatic conditions causes that extreme meteorological events are likely to occur locally as is, for example, evident in the variability of daily landslide risk estimation of the ARI between the stations (Section 4.2.3 & Figure C.3). Drought occurrence in Nepal also varies highly in space, and should, therefore, be estimated on a small scale (Dahal et al., 2016). For improved local information on hazard occurrence throughout the Trishuli catchment generating a full spatial coverage of climatic variables is recommended. Due to the relatively low density of meteorological stations and high climatological variability in Nepal, spatial interpolation techniques between stations are unlikely to provide an appropriate spatial variability. Downscaling of reanalysis data based on a high-resolution digital elevation model (DEM) could, however, potentially provide sufficient spatial variability.

6. Conclusion

The different tools for identifying landslide and drought potential developed in this study can provide useful and comprehendible insights on precipitation deficits and rainfall-triggered landslide risk at different station locations in the Trishuli catchment. These applications are based on a limited number of meteorological variables obtained from reanalysis data that are downscaled through quantile mapping to meteorological station point scale. The subsequent main take-home messages that relate to the subgoals of this study are:

a) Deviations in temperature alone do not have a large impact on crop growth. The computation of a crop specific climatic water balance gives improved insights on water availability and drought potential for crop production of wheat, maize, and paddy in the region. In this computation of the water balance the Makkink method for estimation of evapotranspiration is suggested as most realistic while easy to implement.

b) Antecedent rainfall conditions are essential for the estimation of rainfall-induced landslide occurrence, so an effective method for identifying landslides based on rainfall measurements in the Trishuli catchment is the usage of an antecedent rainfall index (ARI).

c) The visualisations of the climatic water balance and ARI can be published as interactive web applications as a first step for the implementation of accessible early warning tools for drought and landslide occurrence in the catchment of the Trishuli river.

The impact of temperature on crop growth is displayed through the computation of a growing degree day model, resulting in the estimation of the growth stage lengths of rice, wheat, and maize crops. These are estimated to have been very consistent over the past 20 years in Central Nepal. Therefore, delays in crop harvesting are expected to be caused by a reduced water availability related to drought occurrence or other factors that cause crop stresses.

For the computation of drought-related water availability a simple climatic water balance is suggested in which the Makkink method is applied to calculate evapotranspiration. By incorporating the results of the growth stage development to this climatic water balance through adding the crop specific K_c values, an estimation of the cumulative climatic water balance is obtained on field scale for rice, maize, and wheat cultivars in Central Nepal. This allows for monitoring of water availability during crop growth stages that are sensitive to water stress.

Even though many assumptions and empirical parameters are used for estimating growth stage occurrence, the resulting crop calendar is very comparable to the average crop seasons in Nepal. For the subsequent computation of the climatic water balance, it should be considered that evapotranspiration rates are valid under standard conditions. In reality these conditions will, however, deviate. This possibly accounts for the deviations observed when comparing accumulated evaporation over a crop seasonal to lysimeter measurements, which may be improved through calibration of evapotranspiration calculations.

About 95% of the days with landslide events correspond to simultaneous occurrence of precipitation, and a positive trend is found between monthly precipitation and landslide occurrence. This implies that rainfall obtained from the downscaled meteorological dataset

has potential to identify rainfall-triggered landslide risk in the study area. An intensity-duration curve threshold of the Nepalese Himalaya does, however, not represent the relation between rainfall characteristics and landslides correctly in the study area, identifying only 5.7% of all landslides that occurred between 2017-2020. This is possibly due to the neglection of antecedent moisture conditions. Also, limitations in the landslide inventory likely affected the evaluation of rainfall indices.

Incorporating antecedent moisture conditions through estimation of rainfall-induced landslide risk using the ARI methodology result in an improved prediction of landslide potential. Approximately 31% of the landslides that occurred between 2017-2020 were identified by the ARI threshold (TP_{rate}), and 94% of all days between 2017-2020 had a correct estimation of landslide risk (accuracy). The performance of the ARI method for detecting landslides (TP_{rate}) improves by 17% on a lower temporal scale, which implies that implementation of the antecedent rainfall index should possibly be considered on a broader temporal window. This hit rate, however, decreases by 7% when the spatial match of landslides and station location is disregarded, implying that spatial variability affects the performance of the ARI.

To improve information on landslide risk throughout the catchment it is recommended to implement spatial modelling of the climatic variables for a full spatial coverage of the ARI threshold. Also, implementation of the drought applications on a more extensive spatial scale will provide useful information for the communities in the rural regions of the Trishuli catchment. Inaccuracies caused by usage of the downscaled dataset can be avoided through implementation of in situ meteorological observations. Besides, this could provide real-time monitoring and early warning of landslide and precipitation deficit potential, which is beneficial for local hazard awareness and mitigation. As a first step it is, therefore, recommended to implement the visualisations of crop specific water availability and ARI landslide risk as interactive web applications through, for example, the Shiny framework.

References

Aadhar, S., & Mishra, V. (2017). Data Descriptor: High-resolution near real-time drought monitoring in South Asia. *Scientific Data*, *4*(1), 1–14. https://doi.org/10.1038/sdata.2017.145

Allen, R. G., Pereira, L. S., Raes, D., & Smith, M. (1998). Crop evapotranspiration: Guidelines for computing crop requirements. *Irrigation and Drainage Paper No. 56, FAO*, *56*, 300. https://doi.org/10.1016/j.eja.2010.12.001

Ambrosi, C., Strozzi, T., Scapozza, C., & Wegmüller, U. (2018). Landslide hazard assessment in the Himalayas (Nepal and Bhutan) based on Earth-Observation data. *Engineering Geology*, *237*, 217–228. https://doi.org/10.1016/j.enggeo.2018.02.020

Amgain, L. (2011). Accumulated heat unit and phenology of diverse maize varieties as affected by planting dates under Rampur condition, Nepal. *Agronomy Journal of Nepal*, *2*, 111–120. https://doi.org/10.3126/ajn.v2i0.7526

Amgain, L. (2013). Agro- meteorological Indices in Relation to Phenology and Yields of Promising Wheat Cultivars in Chitwan, Nepal. *Journal of Agriculture and Environment*, *14*, 111–120. https://doi.org/10.3126/aej.v14i0.19791

Beguería, S., Vicente-Serrano, S. M., Reig, F., & Latorre, B. (2014). Standardized precipitation evapotranspiration index (SPEI) revisited: Parameter fitting, evapotranspiration models, tools, datasets and drought monitoring. *International Journal of Climatology*, *34*(10), 3001–3023. https://doi.org/10.1002/joc.3887

Bhandari, G. (2011). Estimation of Potential Evapotranspiration and Crop Coefficient of Wheat at Rupandehi District of Nepal. *International Journal of Agricultural Management and Development*, *2*(1), 41–47.

Bhandari, G. (2012). Estimation of Potential Evapotranspiration and Crop Coefficient of Maize at Rupandehi District of Nepal. *International Journal of Agricultural Management and Development (IJAMAD)*, *2*(4), 285–293.

Bhandari, G., & Kayastha, R. B. (2012). Estimation of Crop Coefficient of Rice at Rupandehi District of Nepal. *OIDA International Journal of Sustainable Development*, *4*(6), 47–54.

Bhandari, G., & Panthi, B. B. (2014). Analysis of Agricultural Drought and its Effects on Productivity at Different District of Nepal. *Journal of Institute of Science and Technology*, *19*(1), 106–110. https://doi.org/10.3126/jist.v19i1.13835

BIPAD. (2020). *Damage & Loss*. https://bipadportal.gov.np/damage-and-loss/

Bocchiola, D., Brunetti, L., Soncini, A., Polinelli, F., & Gianinetto, M. (2019). Impact of climate change on agricultural productivity and food security in the Himalayas: A case study in Nepal. *Agricultural Systems*, *171*, 113–125. https://doi.org/10.1016/j.agsy.2019.01.008

Bogaard, T. A., & Greco, R. (2015). Landslide hydrology: from hydrology to pore pressure. *WIREs Water*, *3*(3), 439–459. https://doi.org/10.1002/wat2.1126

Bogaard, T., & Greco, R. (2018). Invited perspectives: Hydrological perspectives on precipitation intensity-duration thresholds for landslide initiation: Proposing hydro-meteorological thresholds. *Natural Hazards and Earth System Sciences*, *18*(1), 31–39. https://doi.org/10.5194/nhess-18-31-2018

Caine, N. (1980). The Rainfall Intensity-Duration Control of Shallow Landslides and Debris Flows. *Geografiska Annaler: Series A, Physical Geography*, *62*, 23–27. https://doi.org/10.1080/04353676.1980.11879996

Central Bureau of Statistics. (2011). *Population Atlas of Nepal | Central Bureau of Statistics, Nepal*. https://cbs.gov.np/catalog/atlas/

Crozier, M. J. (1999). Prediction of rainfall-triggered landslides: A test of the antecedent water status model. *Earth Surface Processes and Landforms*, *24*(9), 825–833. https://doi.org/10.1002/(SICI)1096-9837(199908)24:9<825::AID-ESP14>3.0.CO;2-M

Dahal, P., Shrestha, N. S., Shrestha, M. L., Krakauer, N. Y., Panthi, J., Pradhanang, S. M., Jha, A., & Lakhankar, T. (2016). Drought risk assessment in central Nepal: temporal and spatial analysis. *Natural Hazards*, *80*(3), 1913–1932. https://doi.org/10.1007/s11069-015-2055-5

Dahal, R. K. (2006). *Geology of Nepal*. http://www.ranjan.net.np/index.php/resources/geology-of-nepal

Dahal, R. K. (2014). Regional-scale landslide activity and landslide susceptibility zonation in the Nepal Himalaya. *Environmental Earth Sciences*, *71*(12), 5145–5164. https://doi.org/10.1007/s12665-013-2917-7

Dahal, R. K., Bhandary, N. P., Hasegawa, S., & Yatabe, R. (2014). Topo-stress based probabilistic model for shallow landslide susceptibility zonation in the Nepal Himalaya. *Environmental Earth Sciences*, *71*(9), 3879–3892. https://doi.org/10.1007/s12665-013-2774-4

Dahal, R. K., & Hasegawa, S. (2008). Representative rainfall thresholds for landslides in the Nepal Himalaya. *Geomorphology*, *100*(3–4), 429–443. https://doi.org/10.1016/j.geomorph.2008.01.014

Dalhaus, T., Musshoff, O., & Finger, R. (2018). Phenology Information Contributes to Reduce Temporal Basis Risk in Agricultural Weather Index Insurance. *Scientific Reports*, *8*(1), 46. https://doi.org/10.1038/s41598-017-18656-5

Department of Hydrology and Meteorology. (2020). *Monsoon (June - September 2020) Rainfall Monitoring*.

Department of Hydrology and Meteorology. (2021). *Preliminary Precipitation Summary, Monsoon Season (June-September), 2020*. http://drrportal.gov.np/

Dikshit, A., Satyam, N., & Pradhan, B. (2019). Estimation of Rainfall-Induced Landslides Using the TRIGRS Model. *Earth Systems and Environment*, *3*(3), 575–584. https://doi.org/10.1007/s41748-019-00125-w

Eco-Business. (2020). *Drought and hunger drive Nepal farmers to India, defying Covid ban | News | Eco-Business | Asia Pacific*. https://www.eco-business.com/news/drought-and-hunger-drive-nepal-farmers-to-india-defying-covid-ban/

EM-DAT. (2020). *EM-DAT Disaster Database*. https://public.emdat.be/data

FAO. (2020). *Country profile Nepal, General Introduction*. http://www.fao.org/gender-landrights-database/country-profiles/countries-list/general-introduction/en/?country_iso3=NPL

FAO. (2021). *GIEWS global information and early warning system on food and agriculture | GIEWS Country Brief Nepal*. http://www.fao.org/3/Y4347E/y4347e19.htm

Fawcett, T. (2006). An introduction to ROC analysis. *Pattern Recognition Letters*, *27*(8), 861–874. https://doi.org/10.1016/j.patrec.2005.10.010

Froude, M. J., & Petley, D. N. (2018). Global fatal landslide occurrence from 2004 to 2016. *Natural Hazards and Earth System Sciences*, *18*(8), 2161–2181. https://doi.org/10.5194/nhess-18-2161-2018

Ghimire, Y. N., Shivakoti, G. P., & Perret, S. R. (2010). Household-level vulnerability to drought in hill agriculture of Nepal: Implications for adaptation planning. *International Journal of Sustainable Development and World Ecology*, *17*(3), 225–230. https://doi.org/10.1080/13504501003737500

Ghulam, A., Qin, Q., Teyip, T., & Li, Z. L. (2007). Modified perpendicular drought index (MPDI): a real-time drought monitoring method. *ISPRS Journal of Photogrammetry and Remote Sensing*, *62*(2), 150–164. https://doi.org/10.1016/j.isprsjprs.2007.03.002

Glade, T., Crozier, M., & Smith, P. (2000). Applying probability determination to refine landslide-triggering rainfall thresholds using an empirical "Antecedent Daily Rainfall Model." *Pure and Applied Geophysics*, *157*(6–8), 1059–1079. https://doi.org/10.1007/s000240050017

Government of Nepal. (2021). *Nepal Disaster Risk Reduction Portal*. http://www.drrportal.gov.np/

Guttman, N. B. (1998). Comparing the palmer drought index and the standardized precipitation index. *Journal of the American Water Resources Association*, *34*(1), 113–121. https://doi.org/10.1111/j.1752-1688.1998.tb05964.x

Guzzetti, F., Gariano, S. L., Peruccacci, S., Brunetti, M. T., Marchesini, I., Rossi, M., & Melillo, M. (2020). Geographical landslide early warning systems. In *Earth-Science Reviews* (Vol. 200, p. 102973). Elsevier B.V. https://doi.org/10.1016/j.earscirev.2019.102973

Guzzetti, F., Peruccacci, S., Rossi, M., & Stark, C. P. (2008). The rainfall intensity-duration control of shallow landslides and debris flows: An update. *Landslides*, *5*(1), 3–17. https://doi.org/10.1007/s10346-007-0112-1

Hamal, K., Sharma, S., Nitesh Khadka, |, Gebremeskel Haile, G., Joshi, B. B., Xu, T., & Dawadi, | Binod. (2020). *Assessment of drought impacts on crop yields across Nepal during 1987-2017*. https://doi.org/10.1002/met.1950

Hargreaves, G. H., & Samani, Z. A. (1985). Reference Crop Evapotranspiration from Temperature. *Applied Engineering in Agriculture*, *1*(2), 96–99. https://doi.org/10.13031/2013.26773

Hargreaves, George H., & Allen, R. G. (2003). History and Evaluation of Hargreaves Evapotranspiration Equation. *Journal of Irrigation and Drainage Engineering*, *129*(1), 53–63. https://doi.org/10.1061/(asce)0733-9437(2003)129:1(53)

Hiemstra, P., & Sluiter, R. (2011). Interpolation of Makkink Evaporation in the Netherlands. *De Bilt, 2011 | Technical Report; TR-327*, 78. http://www.numbertheory.nl/files/report_evap.pdf

ICIMOD. (2017). *Nepal Agriculture Atlas*. http://geoapps.icimod.org/agricultureatlas/atlas/

Kafle, K. S. (2017). Disaster Early Warning Systems in Nepal: Institutional and Operational Frameworks. *Journal of Geography & Natural Disasters*, *07*(196), 2167–0587. https://doi.org/10.4172/2167-0587.1000196

Karki, D. B., & Amgain, L. P. (2015). Growth, phenology and yield of drought tolerant rainfed rice cultivars to staggered transplanting dates under changing climatic scenarios of central terai, Nepal. *Journal of the Institute of Agriculture and Animal Science*, 157–164. https://doi.org/10.3126/jiaas.v33i0.20699

Karki, R., Talchabhadel, R., Aalto, J., & Baidya, S. K. (2016). New climatic classification of Nepal. *Theoretical and Applied Climatology*, *125*(3–4), 799–808. https://doi.org/10.1007/s00704-015-1549-0

Keetch, J. J., & Byram, G. M. (1968). A Drought Index for Forest Fire Control. *Research Paper*, *E-38. Ashe*, 35. http://www.treesearch.fs.fed.us/pubs/40

Kirschbaum, D., & Stanley, T. (2018). Satellite-Based Assessment of Rainfall-Triggered Landslide Hazard for Situational Awareness. *Earth's Future*, *6*(3), 505–523. https://doi.org/10.1002/2017EF000715

KNMI. (2018). *Hydrologische droogte zet door*. https://www.knmi.nl/over-het-knmi/nieuws/hydrologische-droogte-zet-door

Liu, X., Xu, C., Zhong, X., Li, Y., Yuan, X., & Cao, J. (2017). Comparison of 16 models for reference crop evapotranspiration against weighing lysimeter measurement. *Agricultural Water Management*, *184*, 145–155. https://doi.org/10.1016/j.agwat.2017.01.017

Liu, Z., Gilbert, G., Cepeda, J. M., Lysdahl, A. O. K., Piciullo, L., Hefre, H., & Lacasse, S. (2021). Modelling

of shallow landslides with machine learning algorithms. *Geoscience Frontiers*, *12*(1), 385–393. https://doi.org/10.1016/j.gsf.2020.04.014
Maraun, D. (2013). Bias correction, quantile mapping, and downscaling: Revisiting the inflation issue. *Journal of Climate*, *26*(6), 2137–2143. https://doi.org/10.1175/JCLI-D-12-00821.1
Maraun, D. (2016). Bias Correcting Climate Change Simulations - a Critical Review. In *Current Climate Change Reports* (Vol. 2, Issue 4, pp. 211–220). Springer. https://doi.org/10.1007/s40641-016-0050-x
Marino, P., Peres, D. J., Cancelliere, A., Greco, R., & Bogaard, T. A. (2020). Soil moisture information can improve shallow landslide forecasting using the hydrometeorological threshold approach. *Landslides*, *17*(9), 2041–2054. https://doi.org/10.1007/s10346-020-01420-8
Mathew, J., Babu, D. G., Kundu, S., Kumar, K. V., & Pant, C. C. (2014). Integrating intensity-duration-based rainfall threshold and antecedent rainfall-based probability estimate towards generating early warning for rainfall-induced landslides in parts of the Garhwal Himalaya, India. *Landslides*, *11*(4), 575–588. https://doi.org/10.1007/s10346-013-0408-2
McAdoo, B. G., Quak, M., Gnyawali, K. R., Adhikari, B. R., Devkota, S., Lal Rajbhandari, P., & Sudmeier-Rieux, K. (2018). Roads and landslides in Nepal: How development affects environmental risk. *Natural Hazards and Earth System Sciences*, *18*(12), 3203–3210. https://doi.org/10.5194/nhess-18-3203-2018
Mcmaster, G. S., & Wilhelm, W. W. (1997). Growing degree-days: one equation, two interpretations Growing degree-days: one equation, two interpretations AGRICULTURAL AND FOREST METEOROLOGY Growing degree-days: one equation, two interpretations. *Agricultural and Forest Meteorology*, *87*, 291–300. https://digitalcommons.unl.edu/usdaarsfacpubhttps://digitalcommons.unl.edu/usdaarsfacpub/83
Miller, P., Lanier, W., & Brandt, S. (2001). *Using Growing Degree Days to Predict Plant Stages E-5*.
Mirus, B. B., Becker, R. E., Baum, R. L., & Smith, J. B. (2018). Integrating real-time subsurface hydrologic monitoring with empirical rainfall thresholds to improve landslide early warning. *Landslides*, *15*(10), 1909–1919. https://doi.org/10.1007/s10346-018-0995-z
Mirus, B. B., Morphew, M. D., & Smith, J. B. (2018). Developing hydro-meteorological thresholds for shallow landslide initiation and early warning. *Water (Switzerland)*, *10*(9), 1–19. https://doi.org/10.3390/W10091274
MoHa. (2017). *Nepal Disaster Report 2017 - The Road to Sendai*.
MoHa. (2019). *Nepal Disaster Report 2019*.
Mokhtari, A., Noory, H., Pourshakouri, F., Haghighatmehr, P., Afrasiabian, Y., Razavi, M., Fereydooni, F., & Sadeghi Naeni, A. (2019). Calculating potential evapotranspiration and single crop coefficient based on energy balance equation using Landsat 8 and Sentinel-2. *ISPRS Journal of Photogrammetry and Remote Sensing*, *154*, 231–245. https://doi.org/10.1016/j.isprsjprs.2019.06.011
Monteith, J. L. (1965). Evaporation and environment. *Symposia of the Society for Experimental Biology*, *19*, 205–234.
Morello, R., De Capua, C., & Lugarà, M. (2013). The design of a sensor network based on IoT technology for landslide hazard assessment. *4th IMEKO TC19 Symposium on Environmental Instrumentation and Measurements 2013: Protection Environment, Climate Changes and Pollution Control*, 99–103.
Morid, S., Smakhtin, V., & Moghaddasi, M. (2006). Comparison of seven meteorological indices for drought monitoring in Iran. *International Journal of Climatology*, *26*(7), 971–985. https://doi.org/10.1002/joc.1264
Mukherjee, S., Mishra, A., & Trenberth, K. E. (2018). Climate Change and Drought: a Perspective on Drought Indices. In *Current Climate Change Reports* (Vol. 4, Issue 2, pp. 145–163). Springer. https://doi.org/10.1007/s40641-018-0098-x
Muñoz-Torrero Manchado, A., Allen, S. A., Ballesteros-c, J. A., Dhakal, A., Dhital, M. R., & Stoffel, M. (2021). Three decades of landslide activit in western Nepal : Unique insights into trends and climate drivers. *Landslides*. https://doi.org/10.1007/s10346-021-01632-6
Nepali Times. (2020). *Nepal's deadliest monsoon in recent times | Nepali Times*. https://www.nepalitimes.com/latest/nepals-deadliest-monsoon-in-recent-times/
Palmer, W. C. (1965). Meteorological Drought. In *U.S. Weather Bureau, Res. Pap. No. 45* (p. 58). https://www.ncdc.noaa.gov/temp-and-precip/drought/docs/palmer.pdf
Pandey, A., & Thongbam, P. (2014). *Rice quality under water stress TSP:Promotion of Agro-based Interventions for Sustainable Livelihood in Nagaland through Tribal Sub Plan View project All India Coordinated Research Network on Potential Crops View project*. www.ijapronline.com
Penman, H. L. (1948). Natural evaporation from open water, bare soil and grass. *Proceedings of the Royal Society of London. Series A. Mathematical and Physical Sciences*, *193*(1032), 120–145.
Petley, D. N., Dunning, S. A., Rosser, N. J., & Hungr, O. (2005). *The analysis of global landslide risk through the creation of a database of worldwide landslide fatalities* (& E. E. O. Hungr, R. Fell, R. Counture (ed.)). Balkema.
Petley, D. N., Hearn, G. J., Hart, A., Rosser, N. J., Dunning, S. A., Oven, K., & Mitchell, W. A. (2007). Trends in landslide occurrence in Nepal. *Natural Hazards*, *43*(1), 23–44. https://doi.org/10.1007/s11069-006-9100-3
R Core Team. (2019). *R: A language and environment for statistical computing*. https://doi.org/10.1016/j.dendro.2008.01.002

Regmi, A. D., Dhital, M. R., Zhang, J. Q., Su, L. J., & Chen, X. Q. (2016). Landslide susceptibility assessment of the region affected by the 25 april 2015 Gorkha earthquake of Nepal. *Journal of Mountain Science*, *7*(2), 725–742. https://doi.org/10.1007/s

Roback, K., Clark, M. K., West, A. J., Zekkos, D., Li, G., Gallen, S. F., Chamlagain, D., & Godt, J. W. (2018). The size, distribution, and mobility of landslides caused by the 2015 Mw7.8 Gorkha earthquake, Nepal. *Geomorphology*, *301*, 121–138. https://doi.org/10.1016/j.geomorph.2017.01.030

Rosser, N., Kincey, M., Oven, K., Densmore, A., Robinson, T., Pujara, D. S., Shrestha, R., Smutny, J., Gurung, K., Lama, S., & Dhital, M. R. (2021). Changing significance of landslide Hazard and risk after the 2015 Mw 7.8 Gorkha, Nepal earthquake. *Progress in Disaster Science*, 100159. https://doi.org/10.1016/j.pdisas.2021.100159

Segoni, S., Piciullo, L., & Gariano, S. L. (2018). A review of the recent literature on rainfall thresholds for landslide occurrence. In *Landslides* (Vol. 15, Issue 8, pp. 1483–1501). Springer Verlag. https://doi.org/10.1007/s10346-018-0966-4

Serraj, R., Kumar, A., McNally, K. L., Slamet-Loedin, I., Bruskiewich, R., Mauleon, R., Cairns, J., & Hijmans, R. J. (2009). Improvement of Drought Resistance in Rice. In *Advances in Agronomy* (Vol. 103, pp. 41–99). Academic Press. https://doi.org/10.1016/S0065-2113(09)03002-8

Shakya, N., & Yamaguchi, Y. (2010). Vegetation, water and thermal stress index for study of drought in Nepal and central northeastern India. *International Journal of Remote Sensing*, *31*(4), 903–912. https://doi.org/10.1080/01431160902902617

Shrestha, M. L. (2000). Interannual variation of summer monsoon rainfall over Nepal and its relation to Southern Oscillation Index. *Meteorology and Atmospheric Physics*, *75*(1–2), 21–28. https://doi.org/10.1007/s007030070012

Shrestha, P. (2019). Nepal, China sign MoU to develop 50-km road linking Kathmandu and Rasuwagadi. *The Kathmandu Post*. https://kathmandupost.com/national/2019/10/14/nepal-china-sign-mou-to-develop-50-km-road-linking-kathmandu-and-rasuwagadi-a-town-bordering-china

Sidle, R. C., & Bogaard, T. A. (2016). Dynamic earth system and ecological controls of rainfall-initiated landslides. *Earth-Science Reviews*, *159*, 275–291. https://doi.org/10.1016/j.earscirev.2016.05.013

Takeuchi, W., Darmawan, S., Shofiyati, R., Khiem, M. V, Oo, K. S., Pimple, U., & Heng, S. (2015). Near-real time meteorological drought monitoring and early warning system for croplands in Asia. *Asian Converence on Remote Sensing 2015: Foresting Resilient Growth in Asia*, *1*, 171–178. http://sharaku.eorc.jaxa.jp/GSMaP

Tallaksen, L. M., & Van Lanen, H. A. J. (2004). Hydrological Drought: Processes and Estimation Methods for Streamflow and Groundwater. In *Development in Water Science* (Vol. 48).

Telegraph Nepal. (2020). *China's Belt and Road Initiative and Nepal – Telegraph Nepal*. http://telegraphnepal.com/chinas-belt-and-road-initiative-and-nepal/

Thapa, P. S., & Adhikari, B. R. (2019). Development of community-based landslide early warning system in the earthquake-affected areas of Nepal Himalaya. *Journal of Mountain Science*, *16*(12), 2701–2713. https://doi.org/10.1007/s11629-019-5586-5

Thomas, M. A., Collins, B. D., & Mirus, B. B. (2019). Assessing the Feasibility of Satellite-Based Thresholds for Hydrologically Driven Landsliding. *Water Resources Research*, *55*(11), 9006–9023. https://doi.org/10.1029/2019WR025577

Thomas, M. A., Mirus, B. B., & Collins, B. D. (2018). Identifying Physics-Based Thresholds for Rainfall-Induced Landsliding. *Geophysical Research Letters*, *45*(18), 9651–9661. https://doi.org/10.1029/2018GL079662

Trenberth, K. E., Dai, A., Van Der Schrier, G., Jones, P. D., Barichivich, J., Briffa, K. R., & Sheffield, J. (2014). Global warming and changes in drought. In *Nature Climate Change* (Vol. 4, Issue 1, pp. 17–22). Nature Publishing Group. https://doi.org/10.1038/nclimate2067

Upreti, B. N. (1999). An overview of the stratigraphy and tectonics of the Nepal Himalaya. *Journal of Asian Earth Sciences*, *17*(5–6), 577–606. https://doi.org/10.1016/S1367-9120(99)00047-4

Van Loon, A. F., Stahl, K., Di Baldassarre, G., Clark, J., Rangecroft, S., Wanders, N., Gleeson, T., Van Dijk, A. I. J. M., Tallaksen, L. M., Hannaford, J., Uijlenhoet, R., Teuling, A. J., Hannah, D. M., Sheffield, J., Svoboda, M., Verbeiren, B., Wagener, T., & Van Lanen, H. A. J. (2016). Drought in a human-modified world: Reframing drought definitions, understanding, and analysis approaches. *Hydrology and Earth System Sciences*, *20*(9), 3631–3650. https://doi.org/10.5194/hess-20-3631-2016

Vicente-Serrano, S. M., Beguería, S., & López-Moreno, J. I. (2010). A multiscalar drought index sensitive to global warming: The standardized precipitation evapotranspiration index. *Journal of Climate*, *23*(7), 1696–1718. https://doi.org/10.1175/2009JCLI2909.1

Vogt, J. V., Neumann, G., Masante, D., Spioni, J., Cammalleri, C., Erian, W., Pischke, F., Pulwarty, R., & Barbosa, P. (2018). Drought Risk Assessment and Management. A conceptual Framework. In *Publication Office of the European Union*. https://doi.org/10.1007/s11269-017-1698-2

Wang, S. Y., Yoon, J. H., Gillies, R. R., & Cho, C. (2013). What caused the winter drought in western nepal during recent years? *Journal of Climate*, *26*(21), 8241–8256. https://doi.org/10.1175/JCLI-D-12-00800.1

Appendix A – Landslide inventory

Incident Date	District	VDC/Municipality	Latitude [°N]	Longitude [°E]	Incident Place
2-4-2017	Chitawan	Chandibhanjyang	27.80595	84.57471	
3-4-2017	Chitawan	Bharatpur	27.67042	84.43845	
14-4-2017	Chitawan	Others	27.86958	84.62612	Ichhakamana-6
18-6-2017	Chitawan	Others	27.86958	84.62612	Ichhakamana-6
22-6-2017	Chitawan	Kathar	27.57000	84.60000	Ichhakamana-6
28-6-2017	Dhading	Nilkantha	27.91298	84.90890	
30-6-2017	Chitawan	Others	27.86958	84.62612	Ichhakamana-6
9-7-2017	Rasuwa	Others	28.15512	85.26102	parbatikund- 3
15-7-2017	Dhading	Others	28.06263	84.92092	Ganga Jamuna-2
17-7-2017	Dhading	Others	28.01193	84.82486	Tripurasundari-6
23-7-2017	Kathmandu	Kageshwori Manahara	27.72393	85.41191	
26-7-2017	Dhading	Others	28.06263	84.92092	Ganga Jamuna-2
30-7-2017	Kathmandu	Gokarneshor	27.76656	85.40661	
2-8-2017	Chitawan	Others	27.86958	84.62612	Ichhakamana-6
3-8-2017	Dhading	Benighat	27.81000	84.76000	
6-8-2017	Rasuwa	Chilime	28.18534	85.30201	Uttaragaya-4
7-8-2017	Dhading	Nilkantha	27.91298	84.90890	
13-8-2017	Chitawan	Others	27.86958	84.62612	Ichhakamana-3
13-8-2017	Chitawan	Others	27.56617	84.49604	Rapti-13
19-8-2017	Chitawan	Others	27.86958	84.62612	Ichhakamana-6
21-8-2017	Dhading	Nilkantha	27.91298	84.90890	
9-9-2017	Rasuwa	Others	28.08186	85.41494	Gosaikund-6
16-2-2018	Dhading	Neelakantha Municipality	27.91170	85.89594	
20-5-2018	Chitawan	Bharatpur Metropolitan City	27.67042	84.43845	
3-6-2018	Chitawan	Ichchhakamana Rural Municipality	27.86945	84.62610	
17-6-2018	Chitawan	Ichchhakamana Rural Municipality	27.86945	84.62610	
17-6-2018	Nuwakot	Kakani Rural Municipality	27.82548	85.24640	
18-6-2018	Kathmandu	Tokha Municipality	27.76984	85.32917	
27-6-2018	Dhading	Gangajamuna Rural Municipality	28.06269	84.92094	
27-6-2018	Dhading	Khaniyabas Rural Municipality	28.05504	84.05504	
27-6-2018	Dhading	Khaniyabas Rural Municipality	28.05504	84.05504	
27-6-2018	Dhading	Netrawati Dabajon Rural Municipality	27.98233	84.52190	
10-7-2018	Nuwakot	Shivapuri Rural Municipality	27.86111	85.35370	
12-7-2018	Nuwakot	Belkotgadhi Municipality	27.83030	85.12292	
12-7-2018	Nuwakot	Bidur Municipality	27.91092	85.14155	
13-7-2018	Rasuwa	Naukunda Rural Municipality	28.01143	85.27342	

14-7-2018	Nuwakot	Tadi Rural Municipality	27.92121	85.30767	
17-7-2018	Nuwakot	Shivapuri Rural Municipality	27.86111	85.35370	
19-7-2018	Nuwakot	Bidur Municipality	27.91092	85.14155	
19-7-2018	Nuwakot	Shivapuri Rural Municipality	27.86111	85.35370	
19-7-2018	Nuwakot	Suryagadhi Rural Municipality	27.94771	85.22963	
19-7-2018	Nuwakot	Tadi Rural Municipality	27.92121	85.30767	
25-7-2018	Dhading	Galchhi Rural Municipality	27.80006	84.99446	
26-7-2018	Rasuwa	Gosaikunda Rural Municipality	28.08186	85.41494	
28-7-2018	Nuwakot	Panchakanya Rural Municipality	27.89760	85.31879	
2-8-2018	Dhading	Benighatrorang Rural Municipality	27.81000	84.76000	
3-8-2018	Rasuwa	Gosaikunda Rural Municipality	28.08186	85.41494	
6-8-2018	Nuwakot	Kakani Rural Municipality	27.82548	85.24640	
6-8-2018	Nuwakot	Suryagadhi Rural Municipality	27.94771	85.22963	
16-8-2018	Rasuwa	Gosaikunda Rural Municipality	28.08186	85.41494	
17-8-2018	Nuwakot	Bidur Municipality	27.91092	85.14155	
17-8-2018	Dhading	Tripurasundari Rural Municipality	28.01207	84.82475	
18-8-2018	Nuwakot	Panchakanya Rural Municipality	27.89760	85.31879	
18-8-2018	Nuwakot	Tadi Rural Municipality	27.92121	85.30767	
18-8-2018	Kathmandu	Tarakeshwor Municipality	27.78638	85.30328	
19-8-2018	Kathmandu	Kageshworimanohara Municipality	27.72393	85.41191	
24-8-2018	Rasuwa	Gosaikunda Rural Municipality	28.08186	85.41494	
24-8-2018	Kathmandu	Nagarjun Municipality	27.73222	85.25668	
26-8-2018	Nuwakot	Shivapuri Rural Municipality	27.86111	85.35370	
27-8-2018	Dhading	Thakre Rural Municipality	27.73852	85.10130	
28-8-2018	Kathmandu	Chandragiri Municipality	27.68971	85.22048	
29-8-2018	Nuwakot	Shivapuri Rural Municipality	27.86111	85.35370	
2-9-2018	Kathmandu	Tarakeshwor Municipality	27.78638	85.30328	
11-9-2018	Chitawan	Ichchhakamana Rural Municipality	27.86945	84.62610	
11-9-2018	Rasuwa	Uttargaya Rural Municipality	27.99185	85.18284	
12-9-2018	Nuwakot	Dupcheshwor Rural Municipality	27.94342	27.94342	
15-9-2018	Rasuwa	Gosaikunda Rural Municipality	28.08186	85.41494	
2-1-2019	Nuwakot	Bidur Municipality	27.91092	85.14155	
21-4-2019	Nuwakot	Kakani Rural Municipality	27.82548	85.24640	Chhamar Chhap
6-6-2019	Dhading	Benighatrorang Rural Municipality	27.81000	84.76000	

20-6-2019	Rasuwa	Gosaikunda Rural Municipality	27.98000	85.93000	Tatopani
22-6-2019	Rasuwa	Gosaikunda Rural Municipality	28.08186	85.41494	Lingling
26-6-2019	Dhading	Galchhi Rural Municipality	27.80006	84.99446	Mahesh Dovan
30-6-2019	Chitawan	Bharatpur Metropolitan City	27.67042	84.43845	17 Kilo
2-7-2019	Dhading	Benighatrorang Rural Municipality	27.81000	27.808000	Badeheremod
2-7-2019	Chitawan	Ichchhakamana Rural Municipality	27.86945	84.62610	Charkilo
3-7-2019	Chitawan	Ichchhakamana Rural Municipality	27.86945	84.62610	Tinkilo
5-7-2019	Rasuwa	Kalika Rural Municipality	27.99615	27.99615	Ghaleganu
6-7-2019	Nuwakot	Shivapuri Rural Municipality	27.86111	85.35370	
8-7-2019	Rasuwa	Gosaikunda Rural Municipality	28.25373	85.36720	Timure
9-7-2019	Rasuwa	Gosaikunda Rural Municipality	27.98000	85.93000	Tatopani
12-7-2019	Dhading	Benighatrorang Rural Municipality	27.81000	27.80800	Baderemod
12-7-2019	Kathmandu	Dakshinkali Municipality	27.62172	85.26181	
12-7-2019	Dhading	Gajuri Rural Municipality	27.77036	84.84634	Daringal
13-7-2019	Dhading	Benighatrorang Rural Municipality	27.80802	84.76907	Talti
15-7-2019	Kathmandu	Dakshinkali Municipality	27.62172	85.26181	Chitradhari
15-7-2019	Kathmandu	Dakshinkali Municipality	27.62172	85.26181	Lamagaun
15-7-2019	Rasuwa	Gosaikunda Rural Municipality	28.08186	85.41494	Lingling
16-7-2019	Dhading	Gangajamuna Rural Municipality	28.06269	84.92094	Kalleri
17-7-2019	Kathmandu	Budhanilkantha Municipality	27.73584	85.36018	Kapan
27-7-2019	Rasuwa	Gosaikunda Rural Municipality	28.25373	85.36720	Timure
27-7-2019	Dhading	Thakre Rural Municipality	27.73852	85.10130	Hapsecharu
6-8-2019	Nuwakot	Kakani Rural Municipality	27.82548	85.24640	Chautis Kilo
21-8-2019	Kathmandu	Budhanilkantha Municipality	27.73584	85.36018	Kapan Paiyutar
23-8-2019	Rasuwa	Gosaikunda Rural Municipality	28.25373	85.36720	Timure
1-9-2019	Nuwakot	Kakani Rural Municipality	27.82548	85.24640	Bahramail
1-9-2019	Kathmandu	Tarakeshwor Municipality	27.74820	85.31112	manmaiju
17-1-2020	Kathmandu	Dakshinkali Municipality	27.62172	85.26181	Syaulibazar
27-3-2020	Dhading	Benighatrorang Rural Municipality	27.80802	84.76907	Bamrang
17-6-2020	Chitawan	Ichchhakamana Rural Municipality	27.86958	84.62612	
20-6-2020	Rasuwa	Gosaikunda Rural Municipality	28.08186	85.41494	Kulung
10-7-2020	Rasuwa	Gosaikunda Rural Municipality	28.25373	85.36720	Timure

19-7-2020	Kathmandu	Kageshworimanohara Municipality	27.72587	85.41177	Magalphadi
20-7-2020	Dhading	Benighatrorang Rural Municipality	27.80802	84.76907	Bhusatar
20-7-2020	Dhading	Gajuri Rural Municipality	27.77036	84.84634	Majhuwa
20-7-2020	Rasuwa	Gosaikunda Rural Municipality	28.08186	85.41494	Kulung
20-7-2020	Dhading	Tripurasundari Rural Municipality	28.01207	84.82475	Golang
21-7-2020	Chitawan	Bharatpur Metropolitan City	27.67042	84.43845	
21-7-2020	Kathmandu	Dakshinkali Municipality	27.62172	85.26181	
21-7-2020	Kathmandu	Tokha Municipality	27.76984	85.32917	Pasidada
24-7-2020	Nuwakot	Belkotgadhi Municipality	27.82544	85.07526	Dui Pipal
24-7-2020	Dhading	Thakre Rural Municipality	27.73700	85.10125	Karkigau
26-7-2020	Nuwakot	Belkotgadhi Municipality	27.83030	85.12292	
30-7-2020	Chitawan	Ichchhakamana Rural Municipality	27.87183	84.60080	Kurintar
1-8-2020	Nuwakot	Bidur Municipality	27.91092	85.14155	Kagunea
1-8-2020	Chitawan	Ichchhakamana Rural Municipality	27.86954	84.62614	Jalbire
1-8-2020	Nuwakot	Kakani Rural Municipality	27.82548	85.24640	
6-8-2020	Nuwakot	Belkotgadhi Municipality	27.83029	85.12288	Tarukaghat
8-8-2020	Chitawan	Ichchhakamana Rural Municipality	27.86945	84.62610	
10-8-2020	Nuwakot	Bidur Municipality	27.91092	85.14155	Kagunea
16-8-2020	Rasuwa	Gosaikunda Rural Municipality	28.08186	85.41494	Medangfedung
17-8-2020	Rasuwa	Gosaikunda Rural Municipality	28.27736	85.37765	Rasuwagadhi
2-10-2020	Kathmandu	Kageshworimanohara Municipality	27.70105	85.38079	Gothatar

Appendix B – Equation sheet of ET_0 models

Equation sheet of Makkink ET_0 (Hiemstra & Sluiter, 2011)

$$ET_0 = c * \frac{\Delta}{\Delta + \gamma} * \frac{R_s}{\lambda * \rho} * 1000 \quad \text{(B.1)}$$

ET_0 = reference evaporation [mm/day]
c = constant [0.65]
Δ = curve of saturation water vapour pressure [kPa/°C] (Eq. B.2)
γ = psychometric constant [kPa/°C] (Eq. B.4)
R_s = daily incoming shortwave radiation [J/m^2/day]
ρ = bulk density of water [1000 kg/m^3]
λ = heat of vaporization [J/kg] (Eq. B.5)

The slope of the saturation vapour pressure curve is calculated as follows:

$$\Delta = 7.5 * \frac{237.3}{(237.3 + T_{mean})^2} * \ln(10) * eo \quad \text{(B.2)}$$

Where e_o is the saturation vapour pressure (kPa) at the daily mean air temperature:

$$e_o(T_{mean}) = 0.6107 * e^{17.27 * \frac{T_{mean}}{237.3 + T_{mean}}} \quad \text{(B.3)}$$

With T_{mean} as the daily mean temperature to which both the psychometric constant (γ) and heat of vaporization (λ) are related:

$$\gamma = 0.0646 + 0.00006 * T_{mean} \quad \text{(B.4)}$$

$$\lambda = (2501 - 2.375 * T_{mean}) * 1000 \quad \text{(B.5)}$$

So, the calculation of Makkink reference evapotranspiration only relies on R_s and T_{mean}, which are measured at the meteorological stations.

Equation sheet Hargreaves ET_0 (Allen et al., 1998; Hargreaves & Samani, 1985)

$$ET_0 = 0.408 * R_a * 0.0023(T_{mean} + 17.8)(T_{max} - T_{min})^{0.5} \quad \text{(B.6)}$$

R_a = extra-terrestrial radiation [33 MJ/m^2/day]
T_{mean} = daily mean temperature [°C]
T_{max} = daily maximum temperature [°C]
T_{min} = daily minimum temperature [°C]

The radiation is converted to mm/day by the conversion factor of 0.408, and 0.0023 is a constant resulting from empirical coefficients. These empirical coefficients have been developed for grass crop reference evapotranspiration compiled in Davis, California, but the method gives in general acceptable estimates for evapotranspiration in a wide range of climates (Hargreaves & Allen, 2003). The incoming extra-terrestrial radiation varies per season and latitude (Figure B.1). For this study, however, R_a is assumed to be constant throughout the year at a rate of 33 MJ/m^2/day as the study area is located at an approximate latitude of 28°N.

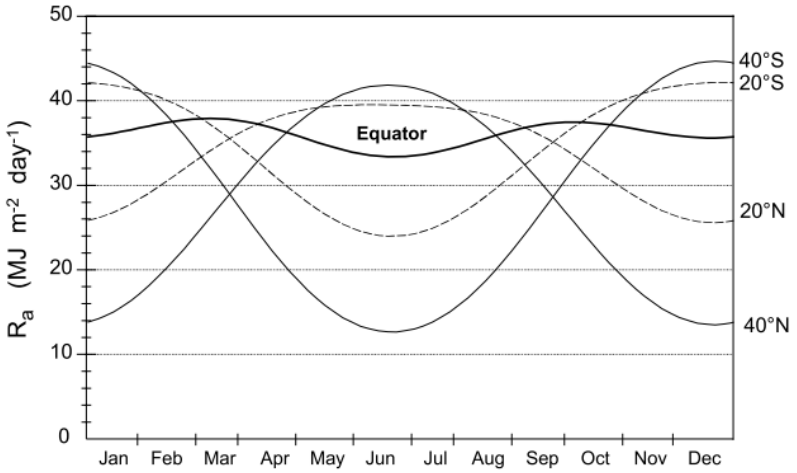

Figure B.1 Annual variation in extra-terrestrial radiation (R_a) at the equator, 20 and 40° (Allen et al., 1998).

Equation sheet of Penman-Monteith ET_0 (Allen et al., 1998)

$$ET_0 = \frac{0.408 * \Delta(R_n - G) + \gamma \frac{900}{T_{mean} + 273} u(e_s - e_a)}{\Delta + \gamma(1 + 0.34u_2)} \quad \text{(B.7)}$$

ET_0 = reference evaporation [mm/day]
Δ = curve of saturation water vapour pressure [kPa/°C] (Eq. B.2)
R_n = net radiation at the crop surface [MJ/m^2/day] (Eq. B.9)
G = soil heat flux [MJ/m^2/day][4]
T_{mean} = daily mean temperature [°C]
u = wind speed [m/s]
e_s = saturation vapour pressure [kPa] (Eq. B.8)
e_a = actual vapour pressure [kPa]
λ = heat of vaporization [J/kg] (Eq. B.5)
γ = psychometric constant [kPa/°C] (Eq. B.13)

The saturation vapour pressure (e_s) is calculated using the following equation:

$$e_s = \frac{e_o(T_{max}) + e_o(T_{min})}{2} \quad \text{(B.8)}$$

Where e_o can be estimated using Eq. B.3 with daily maximum (T_{max}) and minimum (T_{min}) as input instead of daily mean temperatures (T_{mean}).

The net radiation at the crop surface (R_n) is calculated through the difference between net incoming solar radiation (S_n) and the net outgoing longwave radiation (L_n):

$$R_n = S_n - L_n \quad \text{(B.9)}$$

The net incoming shortwave solar radiation (S_n) depends on the albedo (α), which is determined as 0.23 for a hypothetical grass reference crop [-]:

$$S_n = (1 - \alpha)R_s \quad \text{(B.10)}$$

[4] The ground heat flux (G) is very small on daily scale; therefore, the effect of G is ignored (Allen et al., 1998).

The net outgoing longwave solar radiation (L_n) is derived from the Stefan Boltzmann equation and calculated as:

$$L_n = \sigma \frac{(T_{max} + 273.16)^4 + (T_{min} + 273.16)^4}{2} \left(0.34 - 0.14 * \sqrt{e_a}\right) \left(1.35 \frac{R_s}{R_{so}} - 0.35\right) \quad \text{(B.11)}$$

L_n = net outgoing longwave solar radiation [MJ/m^2/day]
σ = Stefan-Boltzmann constant [4.903*10^{-9} MJ/K^4/m^2/day]
e_a = actual vapour pressure [kPa]
R_{so} = clear-sky radiation [MJ/m^{-2}] (Eq. B.12)

Where the clear-sky radiation (R_{so}) is determined using:

$$R_{so} = (0.75 + 2 * 10^{-5} * z) * R_a \quad \text{(B.12)}$$

z = elevation [m]
R_a = extra-terrestrial radiation [33 MJ/m^2/day]

The psychrometric constant [kPa/°C] is determined differently than for the Makkink method, relating to the measured atmospheric pressure:

$$\gamma = \frac{c_p P}{\varepsilon \lambda} = 0.665 * 10^{-3} P \quad \text{(B.13)}$$

γ = psychrometric constant [kPa/°C]
P = atmospheric pressure [kPa]
λ = latent heat of vaporization [2.45 MJ/kg]
c_p = specific heat at constant pressure [1.013*10^{-3} MJ/kg/°C]
ε = ratio molecular weight of water vapour/dry air [0.622]

For this parameterization of the Penman-Monteith equation incoming solar radiation (R_s), wind speed (u), actual vapour pressure (e_a), air pressure (P) and the maximum (T_{max}), minimum (T_{min}) and mean temperatures (T_{mean}) are measured at the monitoring stations. Also, the elevation (z) is given for each station (Table 3.1).

Appendix C – Additional figures

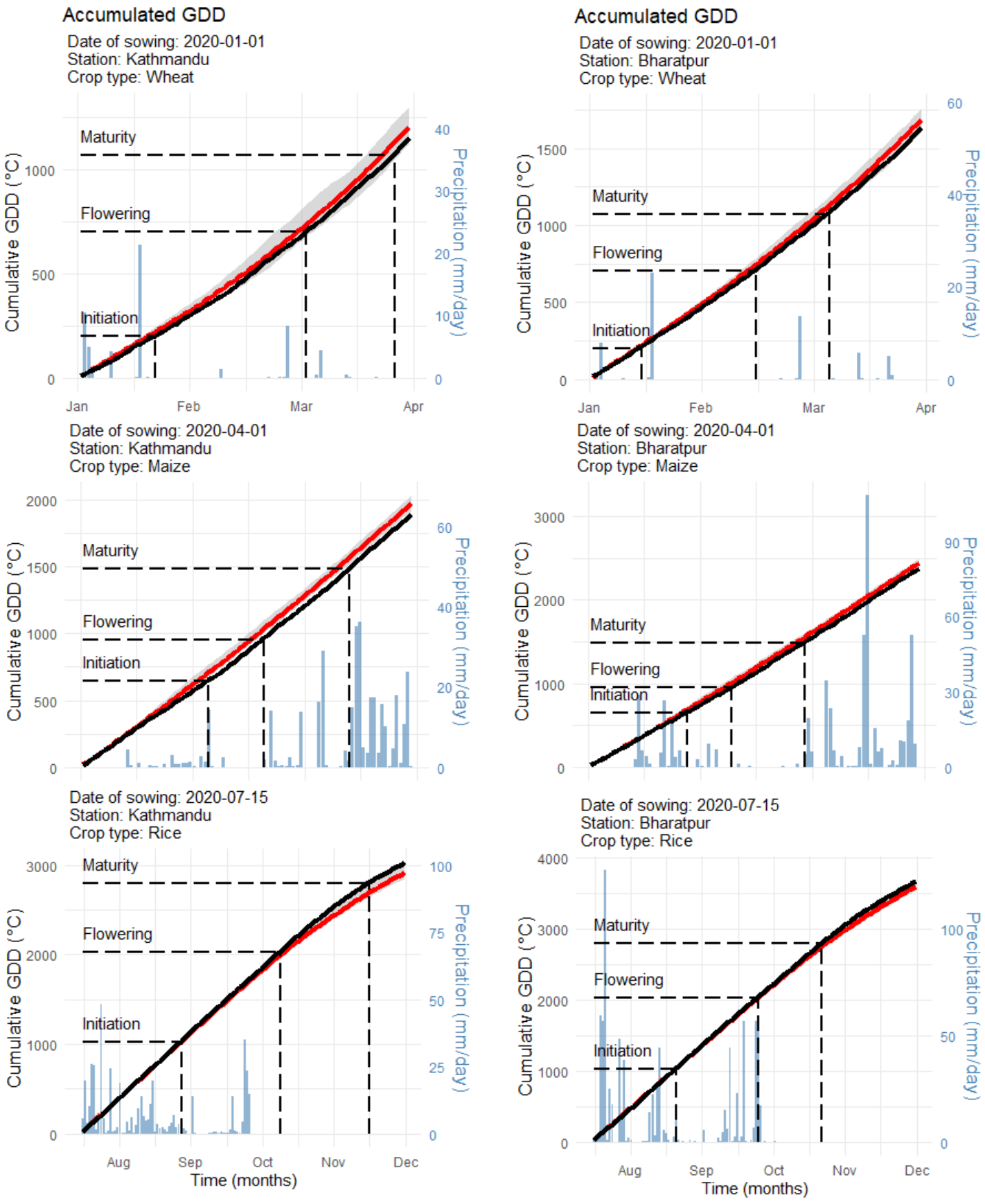

Figure C.1 Cumulative growing degree days [°C] and corresponding growth stage thresholds for wheat (top), maize (middle) and paddy (bottom) crops at Kathmandu (left) and Bharatpur (right) during the respective crop seasons. Precipitation [mm/day] is indicated in blue.

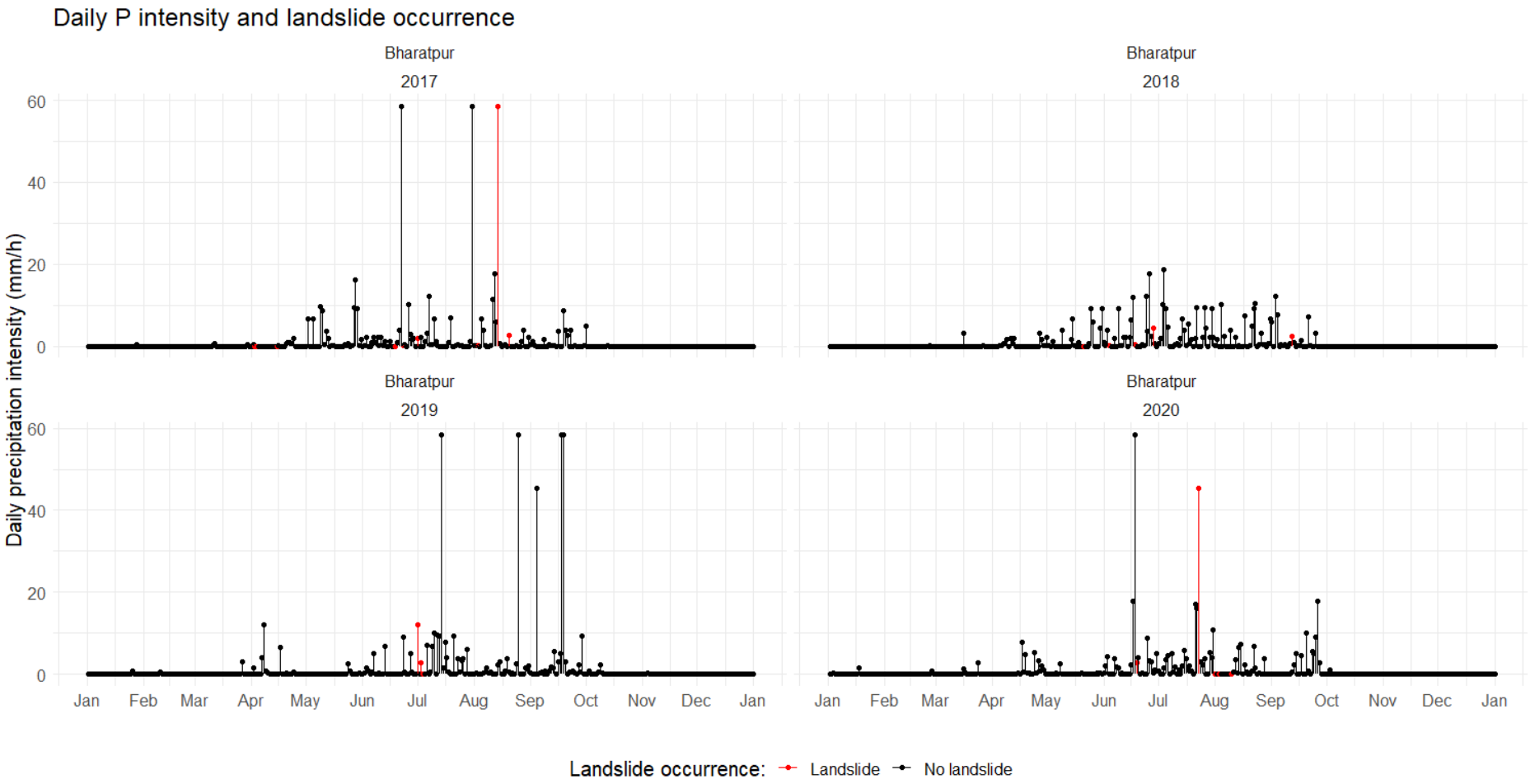

Figure C.2 Maximum daily precipitation intensity [mm/h] and landslide occurrence (red) in proximity to the Bharatpur station from 2017-2020.

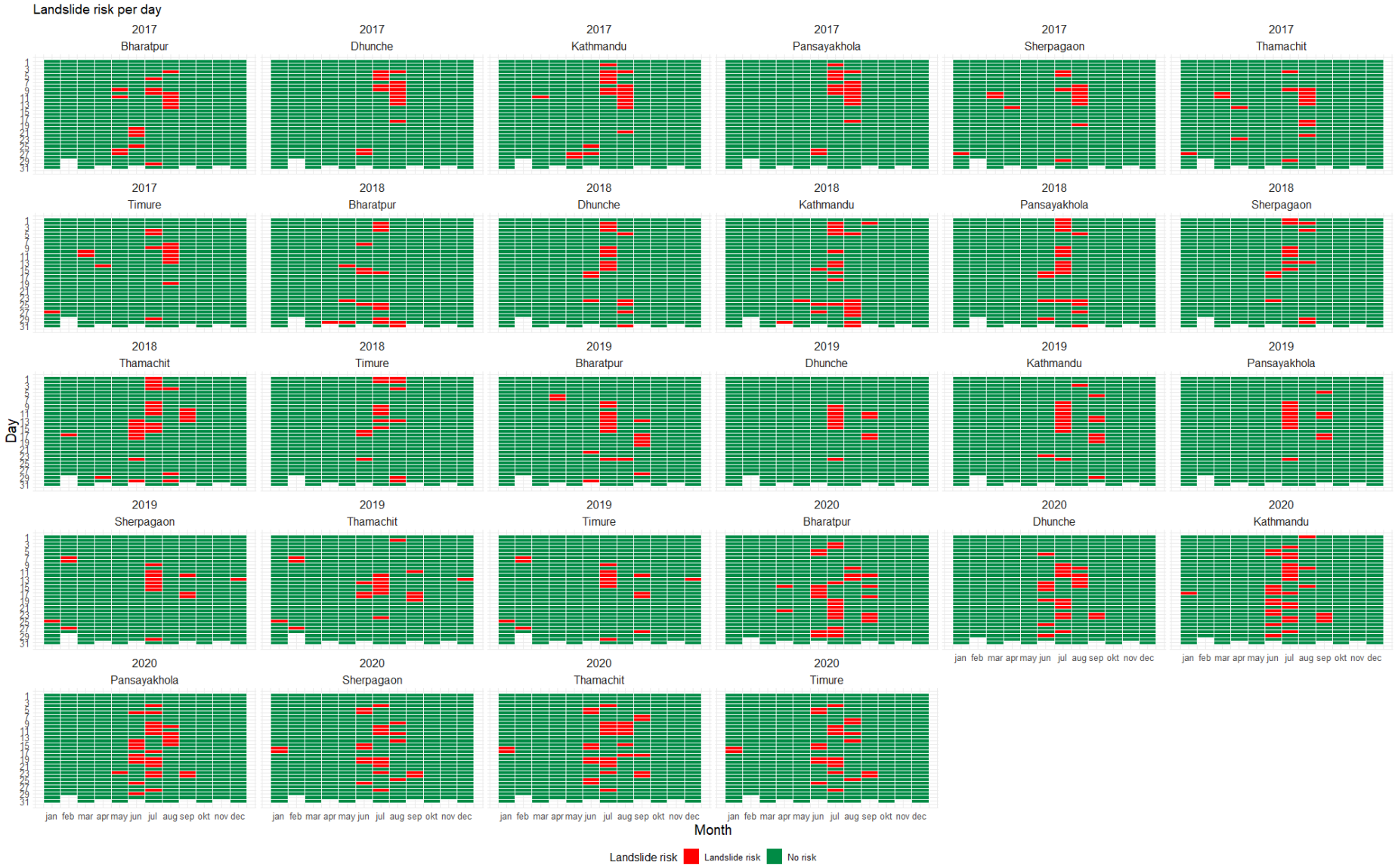

Figure C.3 Daily landslide risk (2017-2020) at Bharatpur, Dhunche, Kathmandu, Pansayakhola, Sherpagaon, Thamachit and Timure as estimated by the ARI.

Figure C.4 Performance of ARI predicted landslide potential at Bharatpur, Dhunche, Kathmandu, Pansayakhola, Sherpagaon, Thamachit and Timure on daily scale compared to the landslide inventory of 2017-2020 (DRR Nepal).